Nature Communications

https://doi.org/10.1038/s41467-026-74063-3

Article in Press

Nanozyme-engineered liners for proactive prevention of wear particle-induced osteolysis

Received: 24 April 2024

Accepted: 20 May 2026

Cite this article as: Liu, S., Zhao, S., Sun, Q. *et al.* Nanozyme-engineered liners for proactive prevention of wear particle-induced osteolysis. *Nat Commun* (2026). https://doi.org/10.1038/s41467-026-74063-3

Shujie Liu, Sheng Zhao, Qi Sun, Quanyi Liu, Yihong Zhang, Yixuan Li, Lifeng Jiang, Tong Li, Jianan Cao, Jiansen Wang, Jingyuan Zhao, Xiaomiao Cui, Jingjing Zhang, Xinkun Ren, Yan Du, Liming Zheng, Qing Jiang & Hui Wei

Nanozyme-Engineered Liners for Proactive Prevention of Wear Particle-induced Osteolysis

Shujie Liu,[1] Sheng Zhao,[1,2] Qi Sun,[1,3] Quanyi Liu,[4,5] Yihong Zhang,[1] Yixuan Li,[6] Lifeng Jiang,[7] Tong Li,[1] Jianan Cao,[1] Jiansen Wang,[1] Jingyuan Zhao,[1] Xiaomiao Cui,[1] Jingjing Zhang[3], Xinkun Ren,[1] Yan Du, [4,5] Liming Zheng,[6,7]* Qing Jiang,[6,8]* Hui Wei[1,3,9,10]*

[1] College of Engineering and Applied Sciences, National Laboratory of Solid State Microstructures, Jiangsu Key Laboratory of Artificial Functional Materials, Nanjing University, Nanjing, Jiangsu, China.

[2] Key Laboratory of Advanced Drug Delivery Systems of Zhejiang Province, College of Pharmaceutical Sciences, Zhejiang University, Hangzhou, Zhejiang, China.

[3] State Key Laboratory of Analytical Chemistry for Life Science, School of Chemistry and Chemical Engineering, Chemistry and Biomedicine Innovation Center (ChemBIC), ChemBioMed Interdisciplinary Research Centre at Nanjing University, Nanjing University, Nanjing, Jiangsu, China.

[4] State Key Laboratory of Electroanalytical Chemistry, Changchun Institute of Applied Chemistry, Chinese Academy of Sciences, Changchun, Jilin, China.

[5] School of Applied Chemistry and Engineering, University of Science and Technology of China, Hefei, Anhui, China.

[6] State Key Laboratory of Pharmaceutical Biotechnology, Division of Sports Medicine and Adult Reconstructive Surgery, Department of Orthopedic Surgery, Nanjing Drum Tower Hospital, The Affiliated Hospital of Nanjing University Medical School, Nanjing, Jiangsu, China.

[7] Department of Orthopedic Surgery, the Second Affiliated Hospital, Zhejiang University School of Medicine, Hangzhou, Zhejiang, China.

[8] Co-innovation Center of Neuroregeneration, Nantong University, Nantong, Jiangsu,

[9] Nanozyme Laboratory in Zhongyuan, Henan Academy of Innovations in Medical Science, Zhengzhou, Henan, China.

[10] NMPA Key Laboratory for Biomedical Optics, Hangzhou, Zhejiang, China.

China.

*Corresponding authors.

E-mails: Liming Zheng, limzheng@zju.edu.cn; Qing Jiang, qingj@nju.edu.cn; Hui Wei, weihui@nju.edu.cn.

Abstract

Wear particle-induced osteolysis (WPO), primarily caused by particles generated from implants under mechanical loading, remains a major barrier to the long-term success of prosthetic implants. Traditional strategies to address WPO have largely focused on reducing wear generation, rather than mitigating the immunostimulatory effects elicited by wear particles. However, the limited scope of mechanical enhancement and the inevitable generation of wear particles shift increasing attention toward biological improvements. Herein, we propose a "proactive preventive" strategy for liner design, aiming to effectively prevent WPO by simultaneously reducing the generation of wear particles and minimizing their immunostimulatory effects. To validate the feasibility of this strategy, we synthesize a model system by incorporating ceria nanozyme into ultra-high molecular weight polyethylene (UHMWPE), referred to as CZPE. Mechanical assessments demonstrate an approximately 32% reduction in wear particle production of CZPE compared with pristine UHMWPE. Moreover, CZPE particles elicit a markedly attenuated immune response compared to PE particles in a male murine model of WPO, including reduced macrophage-mediated inflammation and diminished intramedullary plasma cell infiltration. These effects contribute to a reduction in osteoclastic bone resorption and foreign body reactions. Leveraging these mechanical and biological advantages, our approach offers a promising implant design strategy for WPO prevention.

Introduction

Arthroplasty is an effective therapeutic intervention for end-staged joint pathologies, improving mobility and quality of life for millions of patients worldwide each year[1-3]. The long-term success of arthroplasty is dependent on the stability of prosthetic devices. Despite advancements in prosthetic design and surgical methodologies, wear particle-induced osteolysis (WPO) and subsequent aseptic loosening remain major complications that significantly limit implant longevity[4]. WPO is primarily driven by immune responses to wear particles released from prosthetic under continuous mechanical stress[5]. Within the periprosthetic microenvironment, polyethylene (PE) particles—derived from the articulating surfaces of artificial joints—are the most prevalent and immunostimulatory, due to their size, surface properties, and wear mechanisms[6-8]. These particles initiate a cascade of inflammatory events, including macrophage dysfunction, chronic inflammation, excessive production of reactive oxygen species (ROS), and subsequent periprosthetic osteolysis[5].

Previous efforts have focused on modifying prosthetic materials to reduce wear and mitigate WPO, including methods such as cross-linking[9], surface coatings[6], and antioxidant-doping[10]. While these approaches have made breakthroughs in reducing wear particle generation[6,10], they fail to fundamentally eliminate the inevitable production of particles under long-term mechanical stress[5,9,11,12]. Once generated, these particles trigger immune responses that lead to osteolysis. Although particles generated from vitamin E-doped and surface-coated liners initially alleviate this physiological reaction, their long-term effectiveness is limited by the stoichiometric consumption of vitamin E and degradation of protective coatings[6,13-15]. Despite being implemented clinically as a targeted intervention, these strategies slightly miss the ultimate efficacy goal, leading us to categorize them as “passive preventive” strategies (Supplementary Fig. 1). This classification reflects their underlying mechanism: they respond to mechanical wear by reducing particle generation, but offer limited control over the biological consequences of particle exposure.

These limitations underscore the need for a paradigm shift in prosthetic design—from passively

limiting wear to actively addressing the biological consequences of wear particles. Acknowledging the inevitability of wear particle generation has prompted the development of design strategies. In contrast to passive preventive strategies, we introduce a proactive preventive strategy (Supplementary Note 1) that not only minimizes the generation of wear particles but also actively mitigates their immunostimulatory effects. Specifically, by endowing the wear particles with intrinsic antioxidant activity, this strategy reduces particle-induced ROS production[5], thereby delaying the amplification of inflammatory responses and the disruption of the local immune microenvironment[16,17]. As a result, the proactive preventive strategy aims to extend the duration of host protection by mitigating the immune responses triggered after particle release, ultimately enabling more sustained prevention of WPO.

The core of the proactive preventive strategy is to reduce the ROS-inducing potential of wear particles while improving the mechanical performance of the liner material. To achieve this, it is essential to identify a long-term stable antioxidant to modify UHMWPE. Ceria (CeO_2) nanozymes were selected as the functional filler due to their ability to enhance the mechanical properties of polymers at the nanoscale[18,19], as well as their catalytic capacity to reduce ROS level through the reversible redox cycling between Ce^{3+} and Ce^{4+} [20-22]. To validate the feasibility of this strategy, we developed a proof-of-concept material by incorporating CeO_2 nanozymes into UHMWPE, referred to as CZPE. This was achieved through the *in situ* growth of CeO_2 within the UHMWPE matrix (Fig. 1a).

In this work, we propose a proactive preventive strategy to mitigate the biological effects of inevitable wear particle generation. Guided by this strategy, we develop CZPE by incorporating CeO_2 nanozymes into UHMWPE, which provides improved mechanical strength and intrinsic antioxidant activity. Mechanical assessments show that CZPE reduces the generation of particles under mechanical load. Compared to PE particles, CZPE particles induce lower levels of ROS. The attenuated ROS stimulation contributes to a reduced immune response, less pronounced chronic inflammation, and delayed progression of osteolysis and foreign body reaction (FBR).

Notably, CZPE particles also mitigate bone resorption by suppressing intramedullary plasma cell infiltration. Collectively, these findings demonstrate that CZPE effectively contributes to the prevention of WPO (Fig. 1b).

Results

Fabrication and characterization of bulk CZPE

CZPE was synthesized through *in situ* growth of CeO_2 NPs within the UHMWPE matrix during the dissolving process, using $Ce(acac)_3$ as the organometallic precursor (Fig. 1a)[23]. This synthesis approach enabled CZPE to be mechanically tailored into various implant shapes, as exemplified by the production of a knee joint prosthesis using compression molding and computer numerical control turning techniques (Supplementary Fig. 2). Transmission electron microscopy images showed a homogeneous distribution of CeO_2 NPs within the PE matrix, with an average size of 2.30 ± 0.38 nm. The identified lattice spacing of 0.31 nm, corresponding to the (111) plane of CeO_2 (Supplementary Fig. 3)[24], confirmed the successful incorporation of these NPs. Energy-dispersive X-ray spectroscopy (EDS) analysis showed the similar distribution patterns of cerium (Ce) and carbon (C) in CZPE particles, indicating that the *in situ* synthesis method achieved homogeneous incorporation of CeO_2 NPs within the UHMWPE matrix (Supplementary Fig. 4). X-ray diffraction (XRD) patterns of CZPE displayed characteristic peaks of both CeO_2 and crystalline UHMWPE (Fig. 2a), demonstrating the preservation of their structures after high-temperature processing and compression molding. Specifically, CeO_2 exhibited prominent diffraction peaks at 28.6°, 33.1°, and 47.5° (2θ), corresponding to the (111), (200), and (220) planes, respectively, consistent with the cubic fluorite structure of CeO_2[23]. Meanwhile, UHMWPE retained its well-known crystalline peaks at 21.6° and 24.0° (2θ), which correspond to the (110) and (200) planes of the polymer's orthorhombic crystalline structure[25]. X-ray photoelectron spectroscopy (XPS) analysis confirmed that the surface of CZPE particles contains exposed CeO_2 NPs (Supplementary Fig. 26c)[26]. This surface exposure, resulting from the *in situ* synthesis method that ensures uniform CeO_2 NPs distribution in the UHMWPE matrix, may facilitate rapid ROS interaction under oxidative stress and support catalytic antioxidant activity.

To explore the impact of CeO_2 content on the anti-aging and mechanical properties of CZPE, we fabricated samples with varied CeO_2 mass concentration doping levels: 1% (CZPE-1), 5% (CZPE-5), and 10% (CZPE-10).

Implants possessing anti-aging activity have the potential to exhibit improved oxidative stability and delayed mechanical fatigue[27]. To the end, a four-month oxidation aging test was conducted on these bulk samples at 80 °C after their immersion in squalene, which is equivalent to approximately 6.48 years of actual aging time[27]. Oxidation index, defined as the ratio of C=O to C-H vibration peak areas from Fourier transform-infrared spectra (FT-IR), was employed to evaluate the resistance of the bulk CZPE samples against oxidative deterioration[27]. FT-IR analyses revealed a decrease in the oxidation index with increased CeO_2 content, suggesting that the presence of CeO_2 may contribute to the antioxidant capacity of CZPE. Notably, CZPE-5 and CZPE-10 exhibited a slower increase in the oxidation index after prolonged aging compared to vitamin E-doped UHMWPE (VEPE) (Fig. 2b-d and Supplementary Fig. 5). This anti-aging property of CZPE is likely attributed to the scavenging action of CeO_2 on hydroxyl radicals ($^{\bullet}OH$) generated during the aging process (Supplementary Fig. 6)[27,28].

The mechanical properties of bulk CZPE materials were systematically evaluated through tensile (Fig. 2e), impact (Fig. 2g), and wear tests (Fig. 2i). The tensile tests indicated a noteworthy 23% ($P = 1.09 \times 10^{-5}$) increase in ultimate tensile strength for CZPE-5 compared to PE (Fig. 2f). All CZPE variants maintained their elongation at break and yield strength within the clinically required range for UHMWPE materials (Supplementary Fig. 7)[29]. In the impact resistance evaluation assessed using the notched Izod impact test (Fig. 2h), CZPE-1 and CZPE-5 exhibited increase of approximately 7.5% ($P = 0.0319$) and 15% ($P = 8.07 \times 10^{-5}$) in impact strength, respectively, compared to pristine PE. These mechanical results displayed a consistent trend across different CeO_2 concentrations, initially increasing and then decreasing. CZPE-5 exhibited the most enhancement mechanical properties. The performance of CZPE-1 and CZPE-5 might be related to the combined effects of NP reinforcement, filler-network interaction, and the influence of NPs on

polymer crystallization, particularly at certain concentrations (Supplementary Fig. 8 and Supplementary Table 1)[19,30-32]. However, for CZPE-10, the performances across various mechanical properties were less favorable, potentially due to NP agglomeration at high concentrations and the hindrance of crystallization by the redundant NPs[19,30,31]. Furthermore, the incorporation of CeO_2 in CZPE was associated with improved tribological properties in CZPE-1 and CZPE-5. This enhancement led to a notable reduction in friction coefficient, with reductions of approximately 8% ($P = 6.19 \times 10^{-5}$) for CZPE-1 and 12% ($P = 3 \times 10^{-8}$) for CZPE-5, compared to pristine PE (Supplementary Fig. 9a). The wear tests showed that CZPE-5 had the lowest wear loss rate, approximately 32% ($P = 2.23 \times 10^{-9}$) lower than that of PE (Fig. 2j), and generated less wear debris over multiple cycles (Supplementary Fig. 9b), suggesting potential for reducing the risk of aseptic loosening. The improved wear resistance of CZPE-5 may be related to its increased yield and tensile strengths, which could reduce plastic deformation under shear forces[30]. Additionally, CeO_2 in CZPE may delay the initiation and propagation of cracks through mechanisms such as crack pinning, limiting structural damage to the CZPE surface[33]. Moreover, the influence of CeO_2 NPs on transfer film formation and thermal stability may also contribute to the enhanced wear resistance[18,34]. Following the comprehensive assessment of both antioxidant and mechanical properties, CZPE-5 emerged as the material with the most well-balanced composite characteristics. Building on this, we further explored the physiological performance of CZPE-5.

ROS-scavenging activity of CZPE particles

At the onset of WPO, macrophages encounter the challenges in efficiently phagocytosing and clearing wear particles, which often results in an excessive generation of ROS[35]. These oxidative stress processes disrupt the local immune microenvironment, exacerbating macrophage activation and other immune responses, ultimately contributing to chronic inflammation and periprosthetic osteolysis[5]. Consequently, to simulate particles generated by the mechanical loading of implants during WPO, we mechanically processed bulk CZPE-5 material to obtain CZPE-5 particles. The

focus then shifted to assessing the ROS-scavenging capabilities of the CZPE-5 particles and their efficacy in mitigating the inflammatory processes.

Prior to evaluating their antioxidant ability, we initially excluded the potential influence of endotoxins on the particles using an endotoxin assay kit, ensuring the reliability of our results (Supplementary Fig. 10). Additionally, to more accurately imitate clinical conditions, gradient filtration was used to restrict the particle size to below 10 μm, as particles within this size range are known to elicit significant inflammatory responses (Supplementary Fig. 11 and Supplementary Table 2)[36]. The antioxidant activity of CZPE primarily originates from the CeO_2 nanozymes embedded within the material. CeO_2 exhibits a unique and reversible redox cycling between Ce^{3+} and Ce^{4+} states, which forms the mechanistic basis for its sustained ROS-scavenging capability (Supplementary Fig. 12 and Supplementary Note 4)[21]. To assess the catalytic efficiency of CZPE-5 particles, we examined their scavenging activities against superoxide radical ($O_2^{\bullet-}$) and hydrogen peroxide (H_2O_2), two prominent ROS known for their detrimental role in promoting oxidative stress and disrupting cellular redox signaling (Fig. 3a)[37]. As illustrated in Fig. 3b, CZPE-5 particles exhibited significantly higher superoxide dismutase (SOD)-like activity when compared to PE particles. This enhancement was attributed to their capacity to catalyze the disproportionation of $O_2^{\bullet-}$ into H_2O_2 and O_2[20]. Additionally, an increase in the PE concentration seems to result in a moderate $O_2^{\bullet-}$ scavenging effect. However, this phenomenon is attributable to the inherently robust oxidative properties of $O_2^{\bullet-}$, leading to the detrimental oxidation of a portion of the PE particles, which fundamentally differs from the catalytic degradation of ROS with CZPE. Consequently, when evaluating catalase (CAT)-like activity, which catalyzes the disproportionation of H_2O_2 into O_2 and H_2O[21], no significant change in dissolved oxygen concentration was observed in the PE group as particle concentration increased (Fig. 3c). In contrast, CZPE-5 particles consistently enhanced O_2 levels over time. This suggests that PE particles act merely as substrates undergoing oxidative degradation by ROS, rather than exhibiting catalytic scavenging activity. To evaluate the durability of CeO_2 within the CZPE matrix, CZPE-5 particles were immersed in phosphate-buffered saline (PBS) for one year. Subsequently, the concentration of Ce ions in the supernatant

was quantified using inductively coupled plasma-mass spectrometry (ICP-MS). The results revealed the excellent stability of CZPE-5 particles in simulated *in vivo* conditions (Supplementary Fig. 13). Meanwhile, CZPE-5 particles still exhibited the evident catalytic antioxidant abilities after one-year immersion (Fig. 3d,e). Furthermore, the durability of the ROS-scavenging activity of CZPE-5 particles was evaluated through six consecutive cycles of H_2O_2 decomposition using a supraphysiological concentration of 100 mM. The total mass loss of CeO_2 was approximately 0.04%, indicating excellent resistance to oxidative degradation (Supplementary Fig. 14). Moreover, CZPE-5 particles also exhibited effective H_2O_2-scavenging activity under conditions approximating physiological H_2O_2 levels (Supplementary Fig. 15). Therefore, CZPE-5 particles exhibited sustained and stable antioxidant activity over time.

Reduced pro-inflammatory activity of CZPE particles

To comprehensively assess the cytotoxicity of CZPE-5 particles, we evaluated their effects on three distinct cell types: RAW264.7 macrophages, MC3T3-E1 osteoblastic cells, and murine synovial fibroblasts. A co-culture system was established, where cells and particles were encapsulated within hydrogel spheres to facilitate effective interactions between the cells and particles (Supplementary Fig. 16a)[38]. This 3D system ensured direct contact between cells and particles, thereby simulating a more physiologically relevant microenvironment. The advantages of this 3D alginate bead model are further discussed in Supplementary Note 2. Over a five-day culture period, CZPE-5 particles exhibited significantly lower cytotoxicity than PE particles across all three cell types (Supplementary Fig. 16b-d). These findings underscore the protective role of CeO_2 incorporation, which likely mitigates the deleterious effects of the particles on cell proliferation.

Subsequently, we established an inverted cell model to evaluate ROS levels in macrophages cells and following incubation with various particles (Supplementary Fig. 17a). Utilizing flow cytometry and fluorescence microscopy, we observed a marked decrease in ROS levels of RAW264.7 macrophages exposed to CZPE-5 particles, in contrast to those treated with PE particles (Fig. 3f,g and Supplementary Fig. 17b,c). Notably, a comparable effect was observed in

THP-1-derived macrophages (Supplementary Fig. 17d,e). Collectively, these results demonstrate that, compared to PE particles, CZPE-5 particles not only possess significant ROS-scavenging capability but also effectively reduce macrophage stimulation *in vitro*, thereby attenuating ROS generation. Evaluation of mRNA expression levels of macrophage polarization markers through quantitative real-time polymerase chain reaction (qRT-PCR) revealed differential responses across different macrophage populations under particle stimulation. In RAW264.7 cells, PE particle stimulation led to a significant increased mRNA expression of M1 polarization marker genes *Nos2* (encodes iNOS2) and *Cd86* (encodes CD86), while no significant difference was observed in the mRNA expression of *Mrc1* (encodes CD206, an M2 marker) between the PE and CZPE groups (Supplementary Fig. 18a-c). These results suggest that PE particles promote M1 polarization in RAW264.7 cells, while CZPE particles exhibit a markedly reduced capacity to induce M1 polarization. In contrast, in THP-1-derived macrophages, although CZPE particles still induced a certain level of M1 polarization marker gene expression compared to the Ctrl group, the expression of M1 markers was significantly lower in the CZPE group than in the PE group, accompanied by a marked increase in M2 marker expression (Supplementary Fig. 18d-f). These findings indicated that, compared to the PE particles, CZPE particles exhibit a reduced capacity to promote M1 polarization in THP-1-derived macrophages and concurrently promote their differentiation toward the M2 phenotype. Given the species-specific differences among macrophage populations, these findings highlight the potential for CZPE particles to elicit diverse macrophage responses, underscoring the complexity of their immunomodulatory effects across different cellular environment.

Furthermore, qRT-PCR analysis revealed that although the mRNA expression of pro-inflammatory cytokines, including interleukin-6 (IL-6) (encoded by *Il6*), interleukin-1 beta (IL-1β) (encoded by *Il1b*), and tumor necrosis factor-alpha (TNF-α) (encoded by *Tnf*) was moderately elevated in RAW264.7 macrophages in the CZPE group compared to the Ctrl group, it showed a significantly greater reduction compared to the PE group (Fig. 3h-j). Similar expression differences in the mRNA levels of *IL6* (encodes IL-6), *IL1B* (encodes IL-1β), and *TNF* (encodes TNF-α) were also

noted in THP-1-derived macrophages following CZPE and PE stimulation (Fig. 3k-m). Taken together, these results indicate that although CZPE particles cannot completely eliminate immunological stimulation, they markedly reduce the promotion of macrophage M1 polarization and pro-inflammatory cytokine secretion by scavenging ROS, compared to PE particles. This improvement contributes to the stabilization of the immune microenvironment, thereby playing a beneficial role in the prevention of WPO.

Reduced osteoclastogenic activity of CZPE particles

To investigate the effect of particles on osteoclast differentiation, we used the supernatant from RAW264.7 macrophages stimulated with different particles to induce osteoclastogenesis (Fig. 3n,o). TRAP (tartrate-resistant acid phosphatase) staining revealed that supernatant from PE-stimulated macrophages induced the most pronounced osteoclast differentiation, with a marked increase in osteoclast area compared to the Ctrl group (~725%, $P = 6.10 \times 10^{-9}$), highlighting the strong osteoclastogenic potential of PE particles *in vitro*. In contrast, although the osteoclast area in the CZPE group was also elevated relative to the Ctrl group (~178%, $P = 0.0058$), it was significantly lower than that in the PE group (~66%, $P = 1.46 \times 10^{-7}$). These results suggest that, although CZPE particles do not completely reverse the trend of osteoclast differentiation, they exhibit a markedly reduced osteoclastogenic effect *in vitro* compared to PE particles.

To evaluate the reduced physiological stimulatory effects of CZPE-5 particles *in vivo*, we implanted them in a classic wear particle-induced calvaria osteolysis model (Fig. 3p). Although the CZPE group still exhibited a certain degree of bone resorption compared to the Ctrl group, it demonstrated significant improvement in mitigating bone resorption relative to the PE group. Micro-computed tomography (CT) imaging demonstrated notable alterations in the cranial bone surface morphology in the PE group, characterized by extensive irregular cavities and depressions due to bone resorption (Fig. 3q). In contrast, in the CZPE group, this phenomenon was alleviated, resulting in a reduction of cavities on the calvaria surface. Quantitative analysis of bone volumetric fraction (BV/TV) revealed a significant increase of approximately 16% ($P = 5.23 \times 10^{-5}$) in the

CZPE group compared to the PE group (Fig. 3r). Higher levels in bone mineral density (BMD) of bone volume (BV) and BMD of total volume (TV) were also observed in the CZPE group compared to the PE group, with an approximate increase of 8% (P = 0.0053) in BMD of BV and 10% (P = 0.0070) in BMD of TV (Supplementary Fig. 19). These findings indicate that CZPE particles result in less bone loss than PE particles *in vivo*. Histomorphometric analysis using TRAP staining further confirmed the alleviation of bone resorption in the CZPE group compared to the PE group. Specifically, the percentage eroded surface perimeter (%E. Pm) in the calvaria was reduced by approximately 46% ($P = 1.25 \times 10^{-8}$), and osteoclast density was decreased by approximately 44% (P = 0.0480) in the CZPE group relative to the PE group (Fig. 3s, t and Supplementary Fig. 20), suggesting a diminished pro-osteoclastogenic effect of CZPE. The Masson's trichrome staining revealed that the perimeter of newly formed osteoid (%O. Pm) increased by approximately 39% ($P = 5.55 \times 10^{-8}$) in the CZPE group compared to the PE group (Supplementary Fig. 21). Furthermore, interleukin 1 beta (IL-1β), a key inflammation marker, was evaluated through immunofluorescence staining (Supplementary Fig. 22). The CZPE group exhibited reduced IL-1β levels (~18%, P = 0.0053) compared to the PE group, suggesting a reduction in inflammatory burden in the calvaria tissue. Collectively, these results indicate that although CZPE-5 particles did not completely prevent bone resorption, they exhibited a significantly reduced capacity to promote calvarial osteolysis and inflammation compared to PE particles.

Reduced WPO-inducing potential of CZPE particles

To clarify the distinguished effects of CZPE-5 and PE particles on WPO, we established a femoral distal implant model in ICR mice to simulate the pathophysiological conditions within the articular skeletal environment (Fig. 4a)[39]. Additionally, to simulate the typical clinical pathology observed in prosthetic revisions, where wear and loosening commonly lead to the need for revision surgeries 10-15 years after implantation[40], a 7-week duration was selected for the animal model. This corresponds to approximately 19 years in humans, according to comparative studies of aging

between mice and humans[41].

Micro-CT imaging revealed that the trabecular bone surrounding the titanium intramedullary nails exhibited greater structural integrity in the CZPE group compared to the PE group, indicating a substantial reduction in bone resorption (Fig. 4b). Conversely, the PE group existed a decrease in the relative BV/TV (~29%, $P = 0.0065$), BMD of BV (~14%, $P = 0.0031$) and BMD of TV (~34%, $P = 0.0288$) compared to the CZPE group, suggesting significant bone volume loss (Fig. 4c and Supplementary Fig. 23). TRAP staining revealed visibly smaller TRAP-positive regions in the femoral bone tissue of the CZPE group, indicating less osteolytic damage. This was quantitatively confirmed by a substantial decrease (~66%, $P = 2.76 \times 10^{-5}$) in the %E. Pm compared to the PE group (Fig. 4d,e). The density of osteoclasts in the CZPE group also diminished (~48%, $P = 0.0222$) (Supplementary Fig. 24). In addition, the CZPE group exhibited an approximately 123% ($P = 0.0034$) enhancement in %O. Pm compared to the PE group (Supplementary Fig. 25). These results indicate that, compared to PE particles, CZPE particles induce less bone resorption in the femoral medullary cavity and promote greater new bone formation. This suggests that the reduced immunostimulatory effect of CZPE contributes to the maintenance of bone metabolic homeostasis.

Furthermore, we evaluated the preventive efficacy of CZPE particles versus CeO_2 NPs against WPO in the femoral distal implant model. CeO_2 NPs were synthesized through a wet-chemical method[42], ensuring comparable particle size and Ce^{3+}/Ce^{4+} ratio to those in CZPE, while exhibiting excellent ROS-scavenging capabilities (Supplementary Fig. 26). The preventive effect of CZPE was compared to a combination of PE particles and CeO_2 NPs (PE + CeO_2). At one-week post-injection, both the PE + CeO_2 NPs and CZPE groups exhibited reduced bone resorption compared to the PE group (Supplementary Fig. 27a). However, between weeks 4 and 7, the PE + CeO_2 NPs group exhibited a rapid deterioration in essential bone parameters, including BV/TV, BMD of BV, and BMD of TV, in contrast to the CZPE group (Supplementary Fig. 27b-d). After 7-weeks treatment, the PE + CeO_2 group displayed markedly increased bone resorption compared to the CZPE group, suggesting a diminished *in vivo* preventive effect of free CeO_2 NPs against WPO.

This decline was likely due to the rapid metabolism and clearance of free CeO_2 NPs. In contrast, the femoral tissue of the CZPE group showed a significant increase in Ce content compared to that of the sham group (mice that underwent only medial parapatellar arthrotomy followed by suturing) and PE + CeO_2 group (Supplementary Fig. 28). This suggested that the presence of CeO_2 within the CZPE-5 particles were retained, likely due to the encapsulation by the PE matrix, which reduce the metabolic rate of CeO_2 and prolongs its effectiveness. These results further support the feasibility of our design, as CZPE particles, with an equivalent CeO_2 content, demonstrate improved long-term stability and therapeutic performance within the bone marrow cavity compared to CeO_2 NPs alone. Moreover, due to the sustained antioxidant activity of CZPE particles, they also exhibited a more prolonged capacity to prevent WPO compared to VEPE particles (Supplementary Figs. 27, 29, 30 and Supplementary Note 3).

Polarized light microscopy was employed to examine the distribution of particles in the medullary cavity (Supplementary Fig. 31a,b). This revealed a predominant accumulation of both CZPE-5 and PE particles around the titanium alloy bone nails. Immunofluorescence staining demonstrated higher IL-1β expression in regions containing PE particles compared to those with CZPE-5 particles, with an approximate increase of 40% (P = 0.0158) (Supplementary Fig. 31c,d). The CZPE group demonstrated a pronounced reduced inflammation in the femoral bone marrow cavity, as evidenced by a significant decrease (~36%, P = 0.0002) in IL-1β expression compared to the PE group (Fig. 4f,g). The expression levels of IL-6 (~345%, P = 0.0002) and TNF-α (~189%, P = 0.0007) in the bone marrow cavity were also markedly higher in the PE group compared to the CZPE group (Supplementary Fig. 32), further corroborating the pro-inflammatory effect of PE particles and the reduced immunostimulatory impact of CZPE particles.

FBR is a critical complication post-implantation, primarily resulting from implant-induced inflammation, which impedes bone integration and can lead to implant failure[43]. To evaluate the level of FBR, we utilized Masson's trichrome and immunofluorescence staining to assess the fibrous tissue surrounding titanium bone nails under different particle stimulations. The thickness

of the fibrous capsule (Fig. 4h,i) and the number of α-SMA$^+$ fibroblasts (Fig. 4j,k) served as indicators of FBR severity[44,45]. In the CZPE group, no significant increase in fibrous capsule thickness or α-SMA$^+$ fibroblast numbers was observed compared to the Ctrl group. However, the PE group displayed a significant increase in both fibrous capsule thickness (~161%, $P = 4.05 \times 10^{-6}$) and α-SMA$^+$ fibroblasts count (~223%, $P = 0.0026$) compared with Ctrl group, suggesting an aggravated FBR. This suggests that CZPE-5 particles did not intensify FBR induced by titanium bone nails, thereby potentially contributing to implant stability. Collectively, although CZPE-5 particles did not entirely eliminate their residual immunological burden, they showed a stronger preventive effect against WPO compared to PE particles.

In addition, the CZPE-5 particles exhibited excellent *in vivo* biocompatibility, as evidenced by the absence of significant histological changes in organs in two animal models (Supplementary Fig. 33). After a 49-day *in vivo* exposure to CZPE-5 particles, no obvious accumulation of Ce was detected in the vital organs of mice (heart, liver, spleen, lung, and kidney) (Supplementary Fig. 34).

By suppressing excessive immune reactions and promoting immunoregulatory effects, implants actively support processes of tissue healing and regeneration[46], to further comprehensively investigate the immune microenvironment within the bone marrow cavity with particles stimulated, we conducted transcriptome sequencing analysis to evaluate pathway alterations in femoral tissues. Correlation analysis of gene expression among the three groups revealed that the PE group forms a distinct cluster, diverging from the other two groups (Supplementary Fig. 35). This indicated a similar gene expression pattern in the CZPE and Ctrl groups, in contrast to the divergence observed in the PE group. Additionally, in the PE group, the expression of M1 macrophage-related genes was significantly upregulated compared to the other two groups, indicating enhanced polarization of macrophages towards the M1 phenotype in femoral tissues under PE particle stimulation (Supplementary Fig. 36a). This finding was further corroborated by qRT-PCR analysis, which showed an increase in the mRNA expression of M1 polarization markers (*Nos2* and *Cd86*) in the

PE group compared to the CZPE group. These results reflected the excessive macrophage activation and deterioration of inflammatory response in the PE group (Supplementary Fig. 36b,c). Differential gene expression analysis between CZPE and PE groups further identified an upregulation of inflammation-related genes (such as *Csf3, Cxcl2, Il6, Cxcl3*)[47] and a downregulation of genes associated with myeloid cell homeostasis and erythrocyte development (such as *Ifi206, Rsad2, Alas2, Gata1*)[48] in the PE group (Supplementary Fig. 37). These differences observed between the PE and CZPE groups suggested a disruption of intramedullary immune homeostasis in the PE group, potentially driven by enhanced macrophage M1 polarization and the suppression of erythroid cell differentiation by inflammatory mediators[49], thereby further supporting the attenuated immunostimulatory effect of CZPE-5 particles on the local immune microenvironment. Gene set enrichment analysis (GSEA) further revealed that multiple signaling pathways associated with WPO were significantly activated following PE particle stimulation. These pathways included pattern recognition receptors (PRRs), inflammatory responses, FBR, and osteoclast development[45,51,52]. In contrast, all of these pathways were significantly downregulated in the CZPE group compared to the PE group (Supplementary Fig. 38). Transcriptomic analysis corroborated our above experimental results and further illuminated the reduced immunostimulatory effects of CZPE-5 particles compared to PE particles, thereby contributing to the attenuation of FBR and the progression of bone resorption in femoral tissue. These results collectively demonstrated the preventive efficacy of CZPE-5 particles against WPO.

Preventive effect of CZPE on WPO associated with plasma cell-mediated pathway

Advanced bioinformatic analysis of medullary cell markers revealed distinct differential gene expression patterns related to B lymphocytes between the CZPE and PE groups (Fig. 5a). Notably, the PE group showed an upregulation expression of genes encoding markers, transcription factors, and transcriptional coactivators associated with activated B cell, memory B cell, and plasma cell—a pattern not observed in the Ctrl and CZPE groups. Immunofluorescence staining for CD138 (a plasma cell marker) and B220 (a pan-B cell marker) revealed a significant increase (~80%, P =

0.0284) in the density of $CD138^{+}/B220^{-}$ cells in the femoral bone marrow of the PE group compared to the CZPE group (Fig. 5b,c). QRT-PCR results revealed an upregulation (~880%, $P = 8.21 \times 10^{-7}$) of *Sdc1* (encodes CD138) mRNA expression in the PE group compared with the CZPE group (Fig. 5d). This finding was further validated by Western blot analysis, which demonstrated a higher (~125%, $P = 0.0281$) CD138 protein levels in the PE group (Fig. 5e,f). These findings indicated a reduced activation and infiltration of intramedullary plasma cells in the CZPE group compared to PE group[50]. It is important to highlight that although CZPE alleviated the abnormal intramedullary plasma cell infiltration observed in the PE group, it did not suppress plasma cell levels below the normal physiological baseline. Specifically, in the unstimulated Ctrl group, the expression of *Sdc1*, CD138 protein levels, and the density of $CD138^{+}/B220^{-}$ plasma cells were comparable to—or even slightly lower than—those observed in the CZPE group. These findings suggest that CZPE primarily acts by mitigating pathological immune activation rather than disrupting normal immune homeostasis, indicating that it does not induce systemic immunosuppression.

This phenomenon may be attributed to the reduced pro-inflammatory stimulation of CZPE-5 particles compared to PE particles, which reduce the generation of oxidatively modified autoantigens, thereby preventing antigen-presenting cells such as macrophages from promoting plasma cell activation[51,52]. Moreover, CZPE may reduce plasma cell infiltration by attenuating the activation of inflammatory signaling pathways (Supplementary Figs. 38, 39 and Supplementary Note 5) and downregulating the secretion of pro-inflammatory cytokines such as IL-1β, IL-6, and TNF-α. These cytokines play essential roles in establishing and maintaining plasma cell niches within the bone marrow microenvironment[53,54]. Furthermore, under conditions of immune response activation, innate immune cells such as macrophages can promote plasma cell retention and long-term survival in the bone marrow by enhancing cell adhesion[54,55]. The alleviation of inflammatory conditions may help suppress this process. Therefore, we hypothesize that plasma cell infiltration in the bone marrow microenvironment under WPO conditions is a multifactorial process. It is likely driven by inflammation-induced disruption of tissue homeostasis, along with

complex interactions between plasma cells and innate immune cells, such as macrophages. The reduced intramedullary plasma cell infiltration observed in the CZPE group, compared to the PE group, may result from the lower immunostimulatory effect of CZPE particles and the subsequent cascade of immune responses.

The interaction between B lymphocytes development and bone homeostasis within the bone marrow microenvironment has been well-established. During inflammatory responses, various types of B lymphocytes, including plasma cells, can influence bone homeostasis through diverse mechanisms, such as secreting a variety of cytokines and chemokines that actively promote osteoclastogenesis (Supplementary Fig. 40)[56-58]. Additionally, enhanced bone resorption has been observed in various diseases characterized by B lymphocytes activation and abnormal proliferation of plasma cells, providing clinical evidence for the role of B lymphocytes in driving bone resorption under pathological immune conditions[59-61]. While there are limited clinical studies directly linking PE wear to plasma cell infiltration, there is substantial literature documenting B-lymphocytes activation and differentiation in response to various non-metal implants[62-65]. Therefore, we hypothesized that CZPE-5 particles, through their reduced immunostimulatory effect, contribute to altered B lymphocyte responses. This may alleviate plasma cell infiltration, thereby contributing to the reduction of bone resorption in WPO.

To elucidate the regulatory effects of CZPE-5 particles on plasma cells, we investigated the interaction between plasma cells and bone resorption in the pathological environment of WPO. We developed two refined femoral distal implant models, each with varying plasma cell level, utilizing U266B1 multiple myeloma cells[66] and bortezomib (Fig. 5g,l). U266B1 cells are known to induce the infiltration of plasma cells, while bortezomib is a selective inhibitor of the 26S proteasome in plasma cells[67]. Bortezomib administration decreased the number of $CD138^+$ plasma cells in the bone marrow cavity across all experimental conditions (PE (~48%, $P = 0.0011$), CZPE (~46%, $P = 0.0034$), and Ctrl (~39%, $P = 0.0022$)), confirming its effectiveness in depleting plasma cells (Supplementary Fig. 41). The PE group displayed the most significant reduction. In addition,

bortezomib led to a reduction of thrombocytes counts in peripheral blood (Supplementary Fig. 42). Furthermore, no significant alterations were observed in major organs (Supplementary Fig. 43). Following U266B cell injection, the number of $CD138^+$ plasma cells in the bone marrow cavity of all groups increased (PE (~77%, $P = 0.0009$), CZPE (~120%, $P = 1.74 \times 10^{-5}$), and Ctrl (~127%, $P = 0.0001$)), indicating an enhanced infiltration of plasma cells (Supplementary Fig. 44). Notably, the increase was more pronounced in the Ctrl and CZPE groups compared to the PE group. However, the injection of U266B1 cells led to splenic abnormalities in mice, likely due to the migration of tumor cells, while other essential organs remained mostly unaffected (Supplementary Fig. 45).

Micro-CT analysis revealed the patterns of bone resorption in the femoral regions of mice after the injection of U266B1 cells (Fig. 5h). Accompanied by elevated plasma cell levels, the mice exhibited augmented bone resorption, characterized by a pervasive decrease in BV/TV across the groups, with the extent of decline showing notable variation. Both the Ctrl + U266B1 and CZPE + U266B1 groups maintained a higher BV/TV than the PE + U266B1 group. Both the Ctrl + U266B1 and CZPE + U266B1 groups maintained relatively higher BV/TV values compared to the PE + U266B1 group. Notably, in comparison to their PBS-injected counterparts, both Ctrl + U266B1 and CZPE + U266B1 groups displayed notable reductions in relative BV/TV, with decreases of approximately 24% ($P = 0.0283$) and 23% ($P = 0.0126$), while the PE + U266B1 group did not exhibit a marked decline (Fig. 5i). No significant differences in the BMD of BV were observed across all groups after U266B1 cell injection. Conversely, the BMD of TV exhibited a notable decrease in the Ctrl + U266B1 (~20%, $P = 0.0101$) and CZPE + U266B1 (~18%, $P = 0.0295$) groups, while no comparable change in the PE + U266B1 group (Supplementary Fig. 46). Additionally, TRAP-stained sections indicated that while TRAP-positive osteoclastic regions increased in all experimental groups following the injection of U266B1 cells, the CZPE + U266B1 group demonstrated a comparatively improved pattern in osteoclastic resorption relative to the PE + U266B1 group (Fig. 5j). A marked enlargement in %E. Pm was observed in both Ctrl + U266B1 (~88%, $P = 0.0207$) and CZPE + U266B1 groups (~55%, $P = 0.0235$), compared to their PBS-

treated counterparts. In contrast, the PE + U266B1 group showed no significant %E. Pm augmentation than PE + PBS group (Fig. 5k). These findings suggested that plasma cell proliferation in the WPO context may enhance osteoclastogenic activity. Regardless of the injection of U266B1 cells, the Ctrl and CZPE groups maintained higher bone structural integrity than the PE group. However, the bone resorption exacerbated by U266B1 cells was more pronounced in both the Ctrl and CZPE groups compared to that in the PE group. This enhanced response might correlate with the more substantial plasma cell infiltration observed in the Ctrl and CZPE groups after U266B1 cell injection (Supplementary Fig. 44), suggesting that their previously more stable immune microenvironment experienced a more significant disturbance following the injection of U266B1 cells.

Following bortezomib administration, an increase in femoral trabecular bone mass was evident in all groups, compared to their PBS-treated counterparts (Fig. 5m). The Ctrl + Bortezomib and CZPE + Bortezomib groups exhibited substantial enhancements in BV/TV compared to the PE + Bortezomib group, with increases of approximately 59% (P = 0.0222) and 57% (P = 0.0247), respectively. Notably, the PE + Bortezomib group also demonstrated a notable increase in BV/TV compared to the PE + PBS group, with a significant rise of about 115% (P = 0.0465). Conversely, neither the Ctrl + Bortezomib nor the CZPE + Bortezomib group exhibited a statistically significant increase in relative BV/TV than Ctrl + PBS and CZPE + PBS groups (Fig. 5n). Additionally, the PE + Bortezomib group exhibited significant improvements in both BMD of BV and BMD of TV compared to the PE + PBS group, with respective increases of about 15% (P = 0.0371) and 25% (P = 0.0007). In contrast, the Ctrl and CZPE groups did not show such changes following bortezomib treatment (Supplementary Fig. 47). These findings aligned with TRAP staining observations, which revealed a decrease in TRAP-positive areas in all groups post-bortezomib treatment (Fig. 5o). The PE + Bortezomib group exhibited the most pronounced reduction in %E. Pm, approximately 40% (P = 0.0046), compared to its PBS control counterpart. This pattern was not observed in the Ctrl and CZPE groups following bortezomib treatment (Fig. 5p). Bortezomib treatment facilitated an improvement in osteolytic conditions across all groups,

with the Ctrl + Bortezomib and CZPE + Bortezomib groups showing further restoration of bone structural integrity compared to their respective PBS controls. The intervention with bortezomib notably augmented the preventive efficacy of CZPE-5 particles against WPO. For the PE + Bortezomib group, although the treatment did not completely reverse the damage induced by PE particles, it significantly improved bone resorption levels, showing the greatest improvement compared to that in the Ctrl + Bortezomib and CZPE + Bortezomib groups. This effect suggested that bortezomib has enhanced therapeutic efficacy in the PE group compared to the Ctrl and CZPE groups, potentially due to a higher level of plasma cell infiltration in the PE group prior to drug treatment.

Comprehensive analysis of the above findings indicates that increased plasma cell infiltration plays a critical promotive role in the progression of WPO. Compared to the CZPE + PBS group, the elevated plasma cell levels in the CZPE + U266B1 group attenuated the advantage of CZPE particles in reducing osteoclastogenic potential relative to PE particles, leading to marked bone loss (Fig. 5i,k). Furthermore, bortezomib treatment narrowed the disparities between the PE group and both the Ctrl + PBS and CZPE + PBS groups in terms of BV/TV and %E. Pm (Fig. 5n,p). These suggest that the reduction in plasma cell infiltration induced by bortezomib significantly delays the adverse effects caused by PE particles. Together with above findings, these results support our hypothesis that, compared to PE particles, CZPE-5 particles mitigate the promotion of osteoclast activity by reducing plasma cell infiltration within the bone marrow. This plasma cell–dependent regulatory pathway plays a critical role in the WPO-preventive mechanism of CZPE-5 particles.

Discussion

Aseptic loosening is characterized by a slow and progressive pathological course, with clinical symptoms typically emerging only at the late stages of implant failure[68]. Consequently, early systemic intervention is often not feasible in the absence of a definitive clinical diagnosis. Moreover, no specific pharmacological agents have been approved for the treatment of aseptic loosening to date. Although bisphosphonates have shown partial therapeutic potential, their application is largely limited to adjunctive use before or after surgery and is frequently associated with adverse effects[69]. As a result, revision surgery remains the only effective intervention at advanced stages of aseptic loosening, despite imposing substantial physical and financial burdens on patients[2]. Therefore, improving implant design during prosthesis use to prevent aseptic loosening is of critical importance[5].

Current liner optimization strategies primarily focus on minimizing the release of wear particles. However, none of these approaches can fully eliminate particle generation[5]. Once released, wear particles continuously elicit immune responses, contributing to the pathogenesis of WPO. Accordingly, we categorize these strategies as passive preventive strategies and introduce a proactive preventive strategy that represents a conceptual advancement in liner design. Our strategy addresses the inevitable generation of wear particles by integrating two key functions. First, it reduces the production of wear particles. Second, and more importantly, it endows the particles with antioxidant properties, thereby attenuating their immunostimulatory potential following generation. The integration of these two functions confers this strategy with sustained preventive effects, offering the potential to impede the progression of WPO even in the continued presence of wear debris. Furthermore, unlike treatment strategies initiated after disease onset, this prosthetic design may offer timely protection, actively scavenging ROS generated due to immune system activation upon particle generation.

To validate the feasibility of the proactive preventive strategy, we selected CeO_2 nanozyme as functional filler for UHMWPE. CeO_2 nanozyme possess both polymer reinforcement properties

and enzyme-like catalytic activities. As a proof-of-concept material, CZPE was prepared through the *in situ* growth of CeO_2 within the UHMWPE matrix. Compared to unmodified PE, CZPE exhibited a reduced wear rate. More importantly, although CZPE particles could not completely reverse the progression of WPO, they elicited reduced immunostimulatory effects relative to PE particles. As a result, their detrimental impact on inflammation and bone resorption was significantly mitigated. Additionally, CZPE meets the processing requirements for liners, demonstrating excellent manufacturability. The successful preparation of CZPE aligns with the emerging trend of immunomodulatory implant designs[46,70,71], offering promising prospects for WPO prevention. Importantly, the encouraging prophylactic effects of CZPE in WPO models support further development of this proactive preventive strategy. Building on this foundation, future research directions may involve enhancing the catalytic efficiency of nanofillers, tailoring their size and morphology within the UHMWPE matrix, and extending this design principle to other classes of implantable materials. Critically, the selection of functional fillers must satisfy several stringent and simultaneous requirements: they must be synthesizable within the UHMWPE–solvent system, capable of improving mechanical properties, exhibit long-term antioxidant activity, and maintain excellent biocompatibility. These integrated demands underscore the need for a well-balanced material design approach, rather than one that overemphasizes a single characteristic. In addition, combining the proactive preventive strategy with existing mechanical modification techniques could offer synergistic benefits—further reducing wear rates while attenuating the immunostimulatory potential of wear particles. Through ongoing refinement of material design, we envision that future implants may not only offer effective disease prevention, but also contribute to therapeutic modulation and potentially even reversal of pathological processes.

Compared to PE particles, CZPE particles exhibit reduced immunostimulatory effects, leading to a milder disturbance of the intramedullary immune environment under WPO conditions. Through ROS scavenging, CZPE attenuates the activation of phagocytic cells, such as macrophages, thereby further decreasing pro-inflammatory cytokines secretion and delaying the progression of

chronic inflammation. These combined effects contribute to the alleviation of the FBR and osteolysis around metal implant. In addition, we identified a previously underrecognized aspect of PE particle-induced WPO, namely plasma cell infiltration and its association with bone resorption. Compared to PE particles, CZPE particles exhibited reduced immunostimulatory effects, accompanied by a noticeable reduction in intramedullary plasma cell infiltration. Although the underlying mechanism remains to be elucidated, this effect is likely a downstream consequence of the reduced chronic inflammatory stimulation induced by CZPE. The interaction between innate and adaptive immune systems is intricately regulated, and the attenuated inflammatory stimulation associated with CZPE may contribute to reduced plasma cell infiltration through multiple mechanisms. First, the antioxidative capacity of CZPE particles helps mitigate oxidative stress within the bone marrow cavity. This reduction in oxidative stress decreases the generation of oxidized autoantigens and damage-associated molecular patterns (DAMPs), which in turn diminishes lymphocyte activation[51,72,73]. Additionally, the alleviation of chronic inflammation contributes to a decrease in the production of pro-inflammatory cytokines (such as IL-6, IL-1β, and TNF-α), which are critical for driving the maturation and differentiation of B lymphocytes, and the formation of the plasma cell niche[53,63]. Furthermore, a more regulated immune environment may reduce the stimulation of adaptive immune cells, leading to a decrease in the secretion of plasma cell-specific adhesion molecules and chemokines[54,55]. Consequently, we hypothesize that the reduced inflammatory activity of CZPE particles contributes to a feedback regulation of the adaptive immune system, thereby facilitating the preventive effect against WPO. Meanwhile, we acknowledge that elucidating the mechanism of plasma cell infiltration under PE particle-induced aseptic loosening requires analysis based on clinical specimens, as animal models alone cannot fully replicate the complexity of the disease process. In future work, we aim to further explore the underlying mechanisms and provide a theoretical basis for the optimization of immunomodulatory prosthesis design. Given its capacity to mitigate plasma cell infiltration under WPO conditions, CZPE also holds promise for joint replacement applications in oncology patients, particularly those with multiple myeloma, where intramedullary plasma cell infiltration is

commonly observed[59].

While our current study employed a small-animal model, which is widely accepted in the field of orthopedic research, we fully acknowledge that large-animal models and early-phase clinical studies will be essential steps in advancing CZPE toward clinical translation. The murine model used in this study offers several advantages: it is well-established, accommodates the presence of metallic implants, and captures key biological features of particle-induced aseptic loosening. Moreover, within the 7-week timeframe, we demonstrated that CZPE exhibited better prophylactic performance than conventional PE materials. However, we also recognize the inherent limitations of rodent models, particularly in their inability to replicate the complex biomechanical loading and long-term immunological interactions seen in human joints over decades of prosthetic wear. To bridge this translational gap, future studies must incorporate large-animal models that more closely mimic human joint anatomy, loading conditions, and immune responses. These models will be critical for evaluating the durability of the immunomodulatory effect, assessing prosthesis-bone integration under load-bearing conditions, and verifying long-term biosafety. Ultimately, the initiation of early-phase clinical trials will be indispensable for confirming the safety, biocompatibility, and preventive efficacy of CZPE in human patients. In future work, we aim to progressively transition from small-animal models to large-animal studies and ultimately to clinical research, thereby establishing a critical translational pathway for advancing the proactive preventive strategy toward real-world application.

In summary, by combining mechanical robustness with reduced immunostimulatory effects, our proactive preventive strategy offers valuable insight for future prosthetic design and development.

Methods

Ethical statement

All experimental procedures were conducted in accordance with institutional and national ethical guidelines. Animal protocols were reviewed and approved by the Institutional Animal Care and

Use Committee (IACUC) of Nanjing University (protocol no. IACUC-2209007). Mice were housed under specific pathogen-free (SPF) conditions with controlled environmental parameters (24 ± 2 °C, 40–70% relative humidity, and a 12-h light/dark cycle). Animals had unrestricted access to sterilized chow and water during the entire study period. Humane endpoints were predefined as body weight loss exceeding 20%, severe infection, persistent self-inflicted injury, or fracture displacement/nonunion resulting in impaired mobility. No animals met these criteria prior to the planned experimental termination.

To ensure experimental consistency and animal welfare, standardized anesthesia and euthanasia protocols were applied to all experimental animals. Mice were anesthetized using isoflurane (4% induction, 1.5–2% maintenance in oxygen, RWD Life Sciences, R510-22). The animals were maintained under anesthesia continuously throughout the procedure, during which a heating pad was utilized to maintain their body temperature at 37°C, and they were monitored for any signs of distress. Following the procedure, the health status of the mice was monitored regularly until full recovery. For euthanasia, animals were placed in an induction chamber, and CO_2 was introduced via a flowmeter at a flow rate of 10 L/min. This procedure ensured that the animals lost consciousness steadily within 2–3 minutes. After respiratory arrest was observed in all animals, CO_2 exposure was continued for a minimum of 2 minutes to ensure permanent cessation of life. Finally, death was confirmed through cervical dislocation to ensure full compliance with ethical standards for permanent cessation of life.

Animals

Eight-week-old male Institute of Cancer Research (ICR) mice (Mus musculus; strain: ICR; Swiss background) were purchased from Beijing Vital River Laboratory Animal Technology Co., Ltd. Male NOD-Prkdc^{em1}Il2rg^{em2} (NCG) mice (Mus musculus; strain: NOD-Prkdc^{em1}Il2rg^{em2}; NOD/ShiLtJ background), also aged eight weeks, were purchased from Hangzhou Ziyuan Laboratory Animal Technology Co., Ltd. All *in vivo* experiments were performed using male mice, as WPO and aseptic loosening are not generally regarded as sex-specific processes.

Synthesis of ceria nanozyme-engineered ultra-high molecular weight polyethylene (CZPE)

CZPE composites were obtained by an *in situ* synthesis approach. Ultra-high molecular weight polyethylene (UHMWPE, viscosity-average molecular weight 5,500,000 Da; LL-5040, off-color particle counts not exceeding 40 per 100 squares; Shanghai Lianle Chemical Industry Science and Technology Co., Ltd., 8.00 g) was dissolved in decahydronaphthalene (99%, Macklin, 1.28 L) at 140 °C under stirring for 1 h. All operations involving high temperature (140 °C) and organic solvents were performed in a fume hood with standard protective equipment. Cerium acetylacetonate ($Ce(acac)_3$, 99%, Sigma-Aldrich) solutions in ethanol (EtOH, AR, Yonghua Chemical, 40 mg/mL) were prepared at three dosages (205.38 mg, 1070.13 mg, and 2259.16 mg), corresponding to target CeO_2 contents of 1%, 5%, and 10% (w/w), respectively. The required volumes (5.13 mL, 26.75 mL, and 56.48 mL) of $Ce(acac)_3$ solution were slowly added to the polymer solution and maintained under stirring at 140 °C for 24 h to allow in situ reaction. The resulting mixture was poured into cold methanol (MeOH, 0 °C, ≥99.5%) to precipitate the product. The precipitate was collected, washed with EtOH, filtered, and dried under vacuum. PE samples were prepared in the same way without adding $Ce(acac)_3$.

Characterization of CZPE

Transmission electron microscopy (TEM) images of CZPE were obtained using a Tecnai 12 microscope (Philips) operated at 120 kV. X-ray diffraction (XRD) analysis was performed with diffractometers (Ultima III, Rigaku; D8 Advance, Bruker) equipped with Cu Kα radiation (λ = 1.54056 Å). Elemental mapping was carried out by energy-dispersive X-ray spectroscopy (EDS, Aztec X-MaxN 80, Oxford). X-ray photoelectron spectroscopy (XPS) data were collected on a Nexsa G2 system (Thermo Scientific) using a monochromatic Al Kα source. Differential scanning calorimetry (DSC, STA449F3A, NETZSCH) was applied to examine the crystallization behavior of CZPE and PE. Thermodynamic parameters were obtained from the DSC curves, with the crystallization enthalpy (ΔH_c) determined from the second cooling cycle. The crystallinity of the PE phase was calculated from the crystallization peak area according to equation (1)[74]:

$$X_c(\%) = \frac{\Delta H_c}{(1-\varphi)\Delta H_m} 100 \quad (1)$$

where, ΔH_c is enthalpy of crystallization of the sample, ΔH_m is enthalpy of crystallization for 100% crystalline UHMWPE (293 J/g), and φ is the weight fraction of the CeO_2 in CZPE.

Fabrication of bulk PE and CZPE materials

PE and CZPE containing different CeO_2 concentrations were evenly distributed into stainless steel molds. The powders were first compacted at room temperature to ensure complete filling of the mold cavities. Consolidation was then carried out by compression molding using a hot press (YLJ-HP300, Kejing) at 210 °C and 10 MPa for 15 min. The molded specimens were cooled to ambient temperature at a controlled rate of 5 °C/min.

Fabrication of bulk vitamin E-doped UHMWPE (VEPE) material

Referring to the concentrations used in commercially available vitamin E-doped prosthetic devices, UHMWPE was mixed with vitamin E (≥96%, Aladdin) at a mass fraction of 0.8%[15]. The mixture was subsequently processed by thermal pressing under the same molding conditions applied for bulk CZPE materials.

Tensile strength measurement

Type 1B specimens (n = 5 per group, thickness 4 mm) were prepared from the above materials in accordance with ISO-52775[75]. Tensile tests were conducted at room temperature using a universal testing machine (Instron-1121) with a crosshead speed of 10 mm/min. Stress and strain data were collected at 10 Hz, and engineering stress–strain curves were calculated from the crosshead displacement. Ultimate tensile strength, yield strength, and elongation at break were determined from the curves.

Fracture toughness measurement

Notched Izod specimens (63.5 mm × 12.7 mm × 6.35 mm; n = 5 per group) were prepared with double notches according to ASTM-D256[76]. Tests were performed on an Izod impact tester (XJU-2.75, Chengde Testing Machine Factory). The energy absorbed by the pendulum after fracture was recorded as the impact strength.

Tribological property measurement

PE and CZPE specimens (40 mm × 20 mm × 4 mm; n = 6 per group) were subjected to sliding wear tests on a UMT TriboLab system (Bruker) equipped with a reciprocating ball-on-flat module. Zirconia spheres (4.8 mm diameter, Jinxiang) served as the counterpart material, and each specimen was paired with a new ball. Experiments were performed under controlled laboratory conditions (25 ± 3 °C; relative humidity < 20%). The test parameters were set to a stroke length of 10 mm, an average sliding velocity of ~2.5 cm/min, a total sliding duration of 5400 s, and a constant normal force of 9 N. Friction coefficients were continuously monitored and logged throughout the tests.

The wear volume (W_V) of each sample was expressed as the sum of two contributions[77]:

$$W_V = \Delta x \times A + \pi \frac{d^2}{8} W_1 \quad (2)$$

The first contribution ($\Delta x \times A$) represents the principal wear volume in accordance with ASTM G133[78], obtained by averaging six cross-sectional profiles of the wear scar to determine the cross-sectional area (A), which was then multiplied by the sliding stroke length (Δx). The second contribution ($\pi \frac{d^2}{8} W_1$) corresponds to an edge correction, accounting for the geometry of the track margins through the measured width (d) and depth (W_1). Two-dimensional profiles were acquired with a stylus profiler (Dektak XT, Bruker). The wear rate (W_R) was subsequently derived according to ASTM G133 using the equation:

$$W_R = \frac{W_V}{s \times F} \quad (3)$$

where F denotes the applied normal load and s represents the total sliding distance.

Accelerated aging of bulk PE, CZPE, and VEPE samples

Bulk PE, CZPE, and VEPE specimens were incubated in squalene (Meryer) at 120 °C for 24 h in a convection oven to facilitate penetration of the solvent into the polymer matrix. After treatment, the samples were cooled to room temperature, and residual squalene on the surfaces was removed with absorbent gauze. The specimens were then transferred to a convection oven at 80 °C and aged in air for a total of 4 months.

The equivalence between accelerated and real-time aging was estimated using the ASTM F1980-07 model[79]:

$$Accelerated\ aging\ time = \frac{Desired\ real\ time}{Q_{10}^{\left[\frac{T_{AA}-T_{AMB}}{10}\right]}} \quad (4)$$

where Q_{10} represents the temperature coefficient (assumed as 2), T_{AA} is the accelerated aging temperature (80 °C), and T_{AMB} is the ambient temperature. For the *in vivo* implantation, T_{AMB} was taken as the physiological temperature of 37 °C, and therefore the 4 months accelerated aging time is equivalent to *in vivo* working 6.48 years.

Determination of oxidation stability

Samples were prepared for Fourier transform-infrared spectra (FT-IR) analysis by boiling the aged specimens (n = 6 per group) in hexane (AR, Sinopharm Chemical Reagent Co., Ltd.) at 80 °C for 24 h, followed by vacuum drying for 24 h. FT-IR spectra were collected on a NICOLET iS50 spectrometer (Thermo Scientific), with each spectrum obtained as the average of 32 scans. Oxidation levels were determined in accordance with ASTM F2102, where the oxidation index was calculated as the ratio of the integrated absorbance between 1680–1800 cm^{-1} and 1335–1390 cm^{-1} [80].

Preparation and characterization of particles

Bulk CZPE and PE were processed in a ball mill (MSK-SFM-LN-192, MTI KJ Co., Ltd.) at 50 Hz for 15 h to generate particles. The obtained particles were washed several times with ethanol and separated by sequential filtration using reusable filter units (Nalgene, 300–4000) together with Millipore membranes of 41, 20, 10, 5, and 0.01 μm pore size. Particles with sizes below 10 μm were collected, stored in ethanol, and later used in cell and animal studies. VEPE particles were prepared using the same method. For detailed analysis, additional filtration with 1 μm and 0.01 μm membranes was conducted (n = 5 independent preparations). Particle size and morphology were examined by scanning electron microscopy (SEM, Ultra 55, Zeiss), and quantitative parameters such as equivalent circle diameter (ECD), aspect ratio (AR), and roundness (R) were determined using ImageJ software[81].

Endotoxin levels were evaluated using a chromogenic LAL endotoxin assay kit (Genscript). A sample comprising 2 g of particles was immersed in 5 mL of LPS-free water for 24 h. Sterile filtration was conducted using a 0.22 μm filter head (Millipore) to remove particles. The filtrate was subsequently diluted fivefold with lipopolysaccharide (LPS)-free water. Both the undiluted and diluted solutions were subjected to endotoxin testing.

Preparation and characterization of CeO_2 nanoparticles

CeO_2 nanoparticles (NPs) were synthesized according to a previously reported procedure[42] with minor modifications. In a typical preparation, $Ce(NO_3)_3 \cdot 6H_2O$ (504 mg; 99.5%, J & K Scientific) was dissolved in 20 mL of an ethylene glycol–water mixture (v/v = 1:1) under continuous stirring and heated to 60 °C. After 5 min, aqueous ammonia (4 mL, 28–30%, GR, Nanjing Chemical Reagent Co., Ltd.) was added rapidly, and the mixture was stirred for an additional 3 h. Caution: The use of concentrated ammonia requires handling in a well-ventilated fume hood with appropriate personal protective equipment. The resulting precipitate was separated by centrifugation at 12,000 × g for 5 min, washed several times with deionized water, and then re-

dispersed in water for further use. XPS spectra and TEM images of the CeO_2 NPs were obtained using the instruments described above.

Assessment of valence state self-recovery of CeO_2 NPs after oxidative treatment

To evaluate the valence state self-recovery ability of CeO_2 NPs following oxidative treatment, 10 mM H_2O_2 (≥30%, GR, Sinopharm Chemical Reagent Co., Ltd.) was added to a deionized water solution containing 0.25 mg/mL CeO_2 NPs. The transmittance changes were monitored using a UV–Vis spectrophotometer (UV-3600 Plus, Shimadzu), and photographs were recorded to document visible changes.

Additionally, XPS was conducted on three groups of CeO_2 samples: (i) untreated CeO_2 NPs, (ii) CeO_2 NPs treated with 30% H_2O_2 solution for 2 hours, and (iii) CeO_2 NPs treated with 30% H_2O_2 solution for 2 hours and subsequently stored for 6 days. The Ce^{3+}/Ce^{4+} ratio was quantified to assess the recovery of redox states over time (n = 3 independent experiments).

Measurement of hydroxyl radical scavenging activity

Hydroxyl radicals (•OH) were generated through the Fenton reaction of Fe^{2+} with H_2O_2. The scavenging ability of particles against •OH was examined using electron paramagnetic resonance (EPR, EMX PLUS, Bruker) with 5,5-dimethyl-1-pyrroline N-oxide (DMPO, ≥97%, J&K Chemical) as the spin-trapping agent. The reaction mixture was prepared by dissolving H_2O_2 and DMPO in PBS buffer (10 mM, pH 7.4) containing 0.05% (v/v) poloxamer 188 (10%, Sigma-Aldrich). The reaction was initiated by adding $FeSO_4$ (AR, Sinopharm Chemical Reagent Co., Ltd.) and maintained for 2 min before introducing CZPE or PE particles. After an additional 10 s, the EPR signal intensity was recorded immediately. The final concentrations of H_2O_2, Fe^{2+}, and particles were 2.5 mM, 2.5 mM, and 200 μg/mL, respectively.

Measurement of SOD-Like Activity

The SOD-like activity of particles was evaluated by measuring their ability to scavenge superoxide anions ($O_2^{\bullet-}$), which were generated by light irradiation of riboflavin (98%, Sigma-Aldrich)[82]. The reaction system consisted of 20 μL riboflavin (1.2 mM), 80 μL EDTA-2Na (0.1 M, 99%, Macklin), 30 μL nitrotetrazolium blue chloride (NBT, BR, Sinopharm Chemical Reagent Co., Ltd.) probe (0.1 mg/mL), and 20 μL particle suspensions at concentrations of 1, 2, or 5 mg/mL, mixed with 850 μL PBS buffer (10 mM, pH 7.4) containing 0.05% (v/v) poloxamer 188. The mixture was incubated at 37 °C for 5 min and then irradiated with a 27 W LED lamp for 2 min. Absorbance at 580 nm was subsequently recorded using a microplate reader (Molecular Device) (n = 3 independent experiments).

Following a duration of one year of immersion in PBS buffer, the particles were then tested using the identical SOD-like activity protocols.

The SOD-like activity of CeO_2 NPs was measured according to standard SOD-like activity protocols, with the final concentrations of CeO_2 NPs in the test system set at 20, 40, and 100 μg/mL.

Measurement of CAT-Like Activity

The evaluation of CAT-like activity of the particles was performed through the quantification of their catalytic efficiency in facilitating the decomposition of H_2O_2 to generate O_2. Typically, 1 mg/mL of the particles were added to a reaction mixture comprising 10 mM H_2O_2 in a 10 mM PBS buffer (pH 7.4), containing 0.05% (v/v) poloxamer 188. This particular concentration of poloxamer 188 was selected to optimize the dispersibility of PE and CZPE particles in the PBS medium, thereby reducing potential experimental inaccuracies. The resultant oxygen generation was quantified at specific time intervals of 0, 1.5, and 3 h using an oxygen electrode (SevenExcellence, Mettler Toledo). The final data were obtained by subtracting the background measured in PBS containing 0.05% (v/v) poloxamer 188 and 10 mM H_2O_2 (n = 3 independent experiments).

Subsequent to a duration of one year of immersion in PBS buffer, the particles were then tested

using the identical CAT-like activity protocols.

The CAT-like activity of CeO_2 NPs was measured according to standard CAT-like activity protocols, with the final concentrations of CeO_2 NPs in the test system set at 50 μg/mL.

Stability assessment of CZPE particles and VEPE particles

Typically, 2 g of CZPE-5 particles were immersed in 10 mL of PBS (10 mM, pH 7.4) (n = 4 independent specimens per group). The containers were sealed with parafilm and left at room temperature for one year. Subsequently, 1 mL of the supernatant was diluted with deionized water to a final volume of 10 mL and filtered through a 0.01 μm pore size membrane to remove residual particles. The filtrate was then concentrated to 2 mL and digested with 6 mL of aqua regia on a hot plate at 250 °C until dry. The residue was dissolved in 10 mL of deionized water with ultrasonication. PBS that had been left standing under identical conditions for 1 year served as blank sample. The cerium (Ce) content was quantified using inductively coupled plasma mass spectrometry (ICP-MS, Agilent 7800).

To evaluate the catalytic stability of CZPE-5 particles, 200 mg of CZPE-5 was dispersed in 20 mL of deionized water containing 0.05% (v/v) poloxamer 188. H_2O_2 was then added to achieve a final concentration of 100 mM (n = 3 independent specimens per group). The reaction system was placed on a shaker to proceed under constant agitation. At 24-hour intervals, aliquots of the reaction solution were carefully withdrawn using a syringe to minimize particle loss during sampling. The collected solution was subsequently filtered through a 0.22 μm membrane to remove residual particles. The absorbance of the filtrate at 240 nm was measured using a UV-Vis spectrophotometer (UV-3600Plus, Shimadzu) to quantify the residual concentration of H_2O_2. The extinction coefficient is 43.6 $M^{-1} \cdot cm^{-1}$, measured with a 1 cm path length. Subsequently, the concentration of Ce ions in the supernatant was determined by ICP-MS to evaluate the extent of CeO_2 NPs degradation within CZPE. After each measurement, H_2O_2 was replenished to restore its concentration to 100 mM, while maintaining a constant total reaction volume of 20 mL.

The antioxidant capacity of CZPE-5 particles in 100 μM hydrogen peroxide was assessed following a similar procedure, except that the hydrogen peroxide concentration was determined using a Hydrogen Peroxide Assay Kit (Beyotime, S0038).

The long-term antioxidant activity of VEPE particles was evaluated using the same methodology.

Cytotoxicity test

RAW264.7 (catalog no. SCSP-5036) and MC3T3-E1 (catalog no. SCSP-5218) cell lines were obtained from the Cell Bank of the Chinese Academy of Sciences. For microsphere preparation, RAW264.7 cells were suspended at 6×10^5 cells/mL in 1.5% (w/v) sodium alginate (Sigma Aldrich) containing 0.8 mg/mL particles. The suspension was added dropwise (30 μL per drop) into 100 mM $CaCl_2$ solution (≥96.0%, Sigma Aldrich) to form hydrogel microspheres. The microspheres devoid of particles were fabricated as Ctrl group. Each well of a 12-well plate was seeded with eight microspheres in DMEM (Gibco) supplemented with 10% FBS (Gibco), and the medium was refreshed every two days. For 2D monolayer Ctrl group, the number of RAW264.7 cells equivalent to those in eight microspheres was directly seeded into 12-well plates under identical conditions.

Cell proliferation was assessed at 24, 72, and 120 h using the CCK-8 assay kit (Dojindo, Japan), the optical density (OD) values at 450 nm of different experimental groups were measured using the same procedure (n = 3 biological replicates per group). Briefly, CCK-8 solution was diluted in fresh culture medium at a ratio of 1:10. Then, 1.5 mL of the diluted solution was added to each well of a 12-well plate and incubated at 37 °C in a 5% CO_2 atmosphere for 30 min. After incubation, the absorbance at 450 nm was measured using a microplate reader. The diluted CCK-8 solution incubated under identical conditions without cells was used as the blank group. The ΔOD values for all experimental groups were calculated as follows:

$$\Delta OD = OD_{tested\ group} - OD_{blank} \quad (5)$$

The cytotoxicity assay of the particles on MC3T3-E1 cells was conducted following standard

protocols. MC3T3-E1 cells were dispersed in sodium alginate solution at a concentration of 1×10^6 cells/mL, and then cultured in α-Minimum essential medium (α-MEM) supplemented with 10% FBS.

Primary synovial fibroblasts were isolated from 8-week-old male ICR mice. Animals were euthanized by cervical dislocation and disinfected in 75% ethanol for 5 min. Under aseptic conditions, the skin over the knee joint was removed, and synovial tissue around the hindlimb joint was excised and placed in a sterile dish. The tissue was cut into small pieces and digested with type I collagenase (0.2 mg/mL, Biosharp) in DMEM at 37 °C in a 5% CO_2 incubator for 6 h. After digestion, the suspension was centrifuged at 184 × g for 5 min, and the pellet was resuspended in DMEM supplemented with 10% FBS. Cells were cultured at 37 °C with 5% CO_2, and passage-1 fibroblasts were used for cytotoxicity assays, following the same procedure as for RAW264.7 cells.

In vitro ROS-scavenging effect of CZPE particles

The *in vitro* ROS-scavenging effect of CZPE particles on cells was assessed using the inverted cell model. First, RAW264.7 cells were seeded at a density of 2×10^5 cells per well in a 12-well plate and incubated for 12 h. CZPE and PE particles with concentrations of 0.2, 0.4, and 0.8 mg/mL were then dispersed in DMEM containing 10% FBS. This suspension was added to the wells, ensuring complete filling of each well, and sealed with parafilm. The plate was then inverted to maximize contact between the particles and cells. After 24 h of incubation, the plates were repositioned upright, and the medium containing particles was removed. The wells were washed thrice with PBS to eliminate residual particles. Cells were then incubated with 10 μM dichlorofluorescein diacetate (DCFH-DA, ≥97%, Sigma Aldrich) probe in the dark for 30 min, followed by the detection of intracellular ROS levels using flow cytometry (CytoFLEX, Beckman Coulter) (n = 4 biological replicates per group) and fluorescence microscopy (DMi8, Leica) (n = 5 biological replicates per group). And the gating strategy of Flow cytometry was shown in Supplementary Fig. 48.

THP-1 cell culture and differentiation

THP-1 cells (catalog no. TCHu57, Cell Bank of the Chinese Academy of Sciences, Shanghai, China) were obtained from Nanjing Drum Tower Hospital. Cells were seeded in 6-well plates at a density of 2×10^6 per well and cultured for 12 h. Differentiation was induced by treatment with 100 ng/mL phorbol 12-myristate 13-acetate (PMA, ≥98%, Aladdin) for 48 h. After confirming that suspended THP-1 cells had differentiated into adherent macrophages, the PMA-containing medium was replaced. The resulting macrophages were maintained in RPMI-1640 medium supplemented with 10% FBS for subsequent experiments.

The ROS scavenging effect of CZPE particles on THP-1-derived macrophages was evaluated using a standard protocol, and fluorescence microscopy was employed for detection.

Preparation of particle-stimulated macrophage supernatant

The macrophage supernatant induced by particle stimulation was generated using an inverted cell model, as previously described. The concentration of PE and CZPE particles used in this model was 0.8 mg/mL. After 24 hours of incubation, the plates were returned to an upright position, and the medium containing the particles was carefully collected. Excess particles were removed by centrifugation at 184 × g for 5 min, and the resulting supernatant was aliquoted and stored at -80 °C. Subsequently, the cells that had been stimulated by the particles were harvested, washed three times with PBS, and stored at -80 °C for future use.

Macrophage supernatant was prepared using an inverted cell culture model. PE and CZPE particles were applied at a final concentration of 0.8 mg/mL. After 24 h of incubation, the culture plates were returned to the upright position, and the particle-containing medium was collected. Residual particles were removed by centrifugation at 184 × g for 5 min. The clarified supernatant was divided into aliquots and stored at -80 °C. In parallel, particle-stimulated cells were harvested, rinsed three times with PBS, and preserved at -80 °C for later use.

Culture and Stimulation of U266B1 Cells

U266B1 myeloma cells, sourced from the China Center for Type Culture Collection (catalog no. GDC0325), were cultured in Roswell Park Memorial Institute (RPMI) 1640 medium (with 15% FBS) at 37 °C in a 5% CO_2 incubator. U266B1 cells were plated in six-well plates with 3×10^6 per well with different culture medium, including RPMI 1640 medium and a mixture medium of the RPMI 1640 medium and the supernatant from macrophages stimulated with various particles (1:1 dilution) (n = 3 biological replicates per group). The cells were cultured for four days, with medium changes every two days. Afterward, the cells were collected, washed three times with PBS, and stored at -80 °C for later use.

Osteoclast differentiation

Bone marrow cells were harvested from the femur and tibia of 8-week-old male ICR mice by flushing. Cells were seeded in culture dishes and maintained overnight at 37 °C with 5% CO_2 in α-MEM medium supplemented with 30 ng/mL macrophage colony-stimulating factor (M-CSF) and 10% FBS. After 24 h, non-adherent bone marrow-derived monocytes (BMMs) were collected, washed, and cultured under two conditions: (i) osteoclast medium (α-MEM containing 10% FBS, 50 ng/mL receptor activator of nuclear factor kappa-B ligand (RANKL), and 30 ng/mL M-CSF) and (ii) a 1:1 mixture of osteoclast medium and supernatant from macrophages stimulated with particles (n = 5 biological replicates per group). Medium was refreshed every 2 days, and cultures were continued until multinucleated osteoclasts were visible under the microscope. Osteoclast differentiation was assessed by tartrate-resistant acid phosphatase (TRAP) staining, and osteoclast area was quantified using ImageJ software.

Animal studies

For wear particle-induced calvaria osteolysis model, particles stored in ethanol were filtered through a 0.01 μm membrane and resuspended in sterile FBS to a final concentration of 50 mg/mL

(based on the weight of polyethylene). Eight-week-old male ICR mice were randomly divided into Ctrl, PE and CZPE groups, five mice per group. Mice were anesthetized with isoflurane and subjected to depilation, followed by a surgical incision measuring 2 cm over the calvaria. A 50 μL of suspension containing the particles was injected into the subperiosteal space of the calvarial sutures, followed by suture closure. The Ctrl group received only 50 μL of FBS. Post 14-day period, the animals were euthanized via carbon dioxide asphyxiation for subsequent examinations.

For the distal femur implant model, particles were resuspended in FBS as previously described. Medical-grade titanium alloy bone nails (JIURI), measuring 5 mm in length and 1 mm in diameter, were prepared by immersion in the particle-FBS suspension. Male ICR mice, 8 weeks of age, were randomly divided into Sham, Ctrl, PE, CZPE, VEPE and PE+CeO_2 groups (CeO_2 NPs were dispersed in the PE particle suspension at a concentration of 2.63 mg/mL, which is equivalent to the CeO_2 content in the CZPE suspension), with eighteen mice in each group. These mice were anesthetized with isoflurane and depilated at the unilateral knee joint. A medial parapatellar arthrotomy was performed to expose the knee joint surface. A hole was drilled in the intercondylar fossa, followed by the injection of 20 μL of FBS suspension containing PE particles, CZPE particles, VEPE particles, or PE particles + CeO_2 NPs, respectively. The titanium alloy bone pins were then inserted into the intramedullary canal, oriented parallel to the femoral shaft. An additional 20 μL of the particle-FBS suspension was administered into the hole, which was subsequently sealed with bone wax. The incision was closed with sutures. The Ctrl group underwent the same procedure but received FBS without particles. At 1, 4, and 7 weeks post-surgery, the animals were euthanized using carbon dioxide asphyxiation for subsequent analysis.

For femoral implant model with U266B1 cell injection, eight-week-old male NCG mice were randomly divided into six groups: Ctrl + PBS, Ctrl + U266B1, PE + PBS, PE + U266B1, CZPE + PBS, and CZPE + U266B1 groups, with six mice in each group. As previously detailed, the femoral distal implant model was firstly established in these mice. Commencing 4 weeks following particle implantation, U266B1 cells were intramedullary injected at the implant site in a weekly sequence

over three weeks. The U266B1 cells were prepared by centrifugation at 184 × g for 5 min and resuspended in PBS to a final concentration of 5×10^7 cells/mL. Mice were anesthetized with isoflurane. Subsequently, under the guidance of a portable X-ray machine, 20 μL of the cell suspension was injected into the bone marrow cavity via intramedullary injection in the Ctrl + U266B1, PE + U266B1, and CZPE + U266B1 groups. In Ctrl + PBS, PE + PBS, and CZPE + PBS, 20 μL of PBS was injected at the same site. At 7 weeks after surgery, the animals were euthanized via carbon dioxide asphyxiation for subsequent analysis.

For femoral distal implant model with bortezomib administration, eight-week-old male ICR mice were randomly divided into six experimental groups: Ctrl + PBS, Ctrl + Bortezomib, PE + PBS, PE + Bortezomib, CZPE + PBS and CZPE + Bortezomib groups, with six mice in each group. Follow the procedure described previously, the femoral distal implant model was firstly established. Commencing at week four post-implantation, the mice in Ctrl + Bortezomib, PE + Bortezomib, and CZPE + Bortezomib groups received intraperitoneal injections of 200 μL of PBS containing bortezomib (1 mg/kg, ≥98%, Solarbio) every 4 days for a total of 6 injections. In Ctrl + PBS, PE + PBS, and CZPE + PBS, 200 μL of PBS without bortezomib was intraperitoneally injected. The animals were euthanized via carbon dioxide asphyxiation at 7 weeks after surgery for further analysis.

Micro-CT analysis

After soft tissue removal and fixation in 4% paraformaldehyde, calvarial and femoral samples were scanned using a VivaCT 80 system (SCANCO Medical AG, Switzerland). The scanning conditions were 45 kVp, 177 μA, with a voxel resolution of 15.6 μm. For calvarial samples, the region of interest (ROI) included 400 consecutive slices beginning at the point where the anterior epiphyseal line disappeared. For femoral samples, the ROI was defined as 300 consecutive slices from the proximal area of the distal femoral osteo-epiphysis. Structural parameters were calculated, including bone volume fraction (BV/TV), bone mineral density (BMD) of bone volume (BV), and BMD of total volume (TV).

Histomorphometry measurement

Calvarias and femurs were fixed in 4% paraformaldehyde (Biosharp) for 24 h and decalcified in 10% EDTA solution (AR, Sinopharm Chemical Reagent Co., Ltd.). After dehydration and clearing, tissues were embedded in paraffin and sectioned at 5 μm thickness. Sections were stained with TRAP, hematoxylin and eosin (H&E, Servicebio), and Masson's trichrome (Servicebio). Images were acquired using a Pannoramic MIDI digital slide scanner (3DHISTECH). Each section was derived from an individual mouse.

For the histomorphometry analysis of bone tissue, pathological parameters including bone formation (percentage osteoid perimeter, %O. Pm), bone resorption (percentage eroded surface perimeter, %E. Pm), and osteoclast density (Number of Osteoclasts/Total Area, N.Oc/T.A) were identified and quantified in Masson and TRAP-stained sections as per established protocols[83]. For calvarias, the region of interest (ROI) was defined as the midline suture, with three randomly selected high-power fields per mouse for averaging. For femurs, the ROI was set as the trabecular bone adjacent to the implanted metal nail, with three fields per mouse used for statistical evaluation.

For the analysis of tissue response to implants, fibrous capsule thickness was measured in femoral sections stained with Masson's trichrome. The ROI was the capsule region around the titanium alloy nail. In each group, five mice were included, and six random regions per mouse were analyzed. Capsule thickness was quantified with CaseViewer software. Given the variability in sampling sites among animals, values from individual mice were not averaged; instead, all measurements were presented collectively to compare between groups.

Quantitative real-time polymerase chain reaction (qRT-PCR)

For cell experiments, cells were collected by centrifugation at 184 × g for 5 min (n = 3 biological replicates per group). For tissue samples, femoral bones were harvested seven weeks after implantation of metal nails and particles in the distal femur model (n = 3 biological replicates per

group). After carefully removing the bone nails and trimming excess tissue, only the distal femoral region around the insertion site was retained. Total RNA was isolated using Trizol reagent (Servicebio #G3013). Complementary DNA was synthesized with the SweScript All-in-One RT SuperMix Kit (Servicebio #G3337). qRT-PCR was carried out on an Applied Biosystems StepOne™ real-time PCR system (Thermo Scientific) using Universal Blue SYBR Green qPCR Master Mix (Servicebio #G3326) according to the manufacturer's instructions.

The expression levels of mouse mRNA were normalized to the *Gapdh* gene, while human mRNA expression was normalized to the *GAPDH* gene. The relative abundance of each gene was calculated by subtracting the CT value of each sample for an individual gene from the corresponding CT value of *Gapdh* or *GAPDH* (ΔCT). ΔΔCT values were calculated by subtracting the ΔCT of the reference group from the ΔCT of the experimental group. -ΔΔCT values were then raised to the power 2 ($2^{-\Delta\Delta CT}$) to determine the fold-change in gene expression relative to the reference group. Each experiment was repeated at least three times. The sequences of primer set for mRNA are shown in Supplementary Table 3.

Western blotting

Tissue samples were collected as described for the qRT-PCR experiment. Each sample was placed in a 1.5 mL enzyme-free tube, followed by the addition of 300 μL of a complete working lysis buffer containing RIPA lysis buffer (Servicebio #G2002), phosphatase inhibitor cocktail (Servicebio #G2007), and protease inhibitor cocktail (Servicebio #G2006). Homogenization was performed with a SWE-FP high-speed tissue grinder (Servicebio). The lysates were incubated at 4 °C for 40 min, then centrifuged at 13,871 × g for 5 min at 4 °C, and the supernatant was collected. Protein extracts were mixed with 5× SDS-PAGE loading buffer (Servicebio #G2075) and heated at 100 °C for 5 min before storage. Proteins were separated on 15% SDS-PAGE gels and transferred to PVDF membranes. Membranes were blocked in PBST (PBS with 0.1% Tween 20) containing 5% non-fat milk at room temperature for 1 h, followed by overnight incubation at 4 °C with primary antibodies. After washing, membranes were incubated for 2 h at room temperature

with HRP-conjugated goat anti-rabbit IgG (Beyotime #A0208, 1:1000) in PBST containing 1% non-fat milk. Protein bands were detected using an ECL kit (Servicebio #G2014) and visualized with a Tanon 5200 Multi Chemiluminescent Imaging System (Tanon). Band intensities were quantified with ImageJ software. For Western blot quantification, the value for each independent biological replicate was derived from its corresponding technical replicates. Antibodies were as follows: primary antibody against CD138 (Rabbit, Abcam #ab128936, EPR6454, 1:3000), recombinant antibody against IKBα (Mouse, Servicebio #GB151509, SB90, 1:1000), recombinant antibody against phospho-IKBα (Rabbit, Servicebio # GB15212, SB188, 1:500), and recombinant anti-beta actin (β-actin) antibody (HRP conjugated, Servicebio ZB15001-HRP, AC-15, 1:1000).

Immunofluorescence staining and analysis

Paraffin-embedded tissue sections (5 μm) were mounted on glass slides and dried at 42 °C overnight. Slides were deparaffinized, rehydrated, and subjected to heat-mediated antigen retrieval in 10 mM sodium citrate buffer (pH 6). After three washes in PBS, nonspecific binding was blocked with 3% bovine serum albumin in PBS for 1 h. Slides were then incubated in the dark with primary antibodies at room temperature for 8 h: anti-IL-1β (Rabbit, Servicebio #GB11113, 1:800), anti-CD138 (Rabbit, Abcam #ab128936, EPR6454, 1:1000), anti-B220 (Rabbit, Servicebio #GB113886, 1:300), anti-IL-6 (Rabbit, Servicebio #GB11117, 1:500), anti-TNF-α (Rabbit, Servicebio #GB11188, 1:200), anti-α-SMA (Rabbit, Servicebio #GB111364, 1:300), and anti-γ-H2AX (Servicebio #GB111841, 1:200). After washing, sections were incubated for 1 h with the appropriate secondary antibodies and counterstained with DAPI (Servicebio #G1012). Slides were washed again, then cover-slipped. Stained sections were scanned using a Pannoramic MIDI slide scanner. Each section represented an individual mouse. For IL-1β, IL-6, and TNF-α quantification, ROIs were defined as described previously, with three randomly selected high-power fields per mouse used for statistical analysis. Fluorescence intensity was measured using ImageJ software. For $CD138^{+}/B220^{-}$ cell density, the ROI was the bone marrow cavity surrounding the metal implant, while $\alpha\text{-}SMA^{+}$ cell density was measured in the fibrous tissue adjacent to the

implant. Fluorescence intensity, cell counts, and ROI areas were quantified using ImageJ software.

Particle distribution analysis

The distribution of CZPE and PE particles in femoral sections stained with H&E was examined using a polarizing microscope (Eclipse LV100N POL, Nikon). To distinguish particles from potential artifacts, the following criteria were applied: (i) poor visibility or unclear outline under bright field; (ii) strong birefringence with a silver-white appearance but no dichroism under polarized light; (iii) presence within or adjacent to histiocytes; and (iv) localization within the focal plane of the cytoplasm. Each section represented one mouse.

For biodistribution analysis, key organs (heart, liver, spleen, lung, and kidney) as well as femurs were collected, air-dried, and weighed (n = 5 per group). Samples were digested in aqua regia and analyzed by inductively coupled plasma optical emission spectrometry (ICP-OES; iCAP 7200, Thermo / Avio 220 Max, PerkinElmer). Ce levels in visceral organs were normalized to tissue weight, whereas Ce content in femurs was expressed relative to the whole bone mass.

Biocompatibility assessment

To evaluate the biocompatibility of CZPE, major organs (heart, liver, spleen, lung, and kidney) were collected from mice after treatment (n = 3 per group). Tissues were sectioned and stained with H&E, and images were acquired using a Pannoramic MIDI slide scanner. The sections were examined for inflammatory responses and tissue morphology. The same procedure was used to assess visceral changes induced by bortezomib administration and U266B1 cell injection.

Evaluation of bortezomib toxicity on peripheral blood cells

Eight-week-old male ICR mice received intraperitoneal injections of 200 μL PBS containing bortezomib (1 mg/kg) (n = 3 per group). Mice injected with PBS alone served as the Sham group. Injections were given once every four days, for a total of six doses. One day after the final injection,

peripheral blood was collected from the orbital sinus using a capillary tube and transferred to anticoagulant tubes. Blood cell counts were measured with an automated hematology analyzer (BC-2800vet, Mindray).

Transcriptome sequencing and data analysis

Femurs from mice in the distal femoral implant model were collected, and surrounding soft tissues were carefully removed. The distal femoral segment surrounding the bone nail was collected for transcriptome sequencing (n = 3 per group). Sequencing was performed by Shanghai OE Biotech Co., Ltd. (Shanghai, China). Total RNA was extracted using the RNeasy Lipid Tissue Mini Kit (QIAGEN, 74804) following the manufacturer's instructions. RNA concentration and purity were assessed with a NanoDrop 2000 spectrophotometer (Thermo Scientific), and RNA integrity was determined using a 2100 Bioanalyzer (Agilent). Libraries were generated with the VAHTS Universal V6 RNA-seq Library Prep Kit for Illumina (NR604, Vazyme) and sequenced on an Illumina Novaseq 6000 platform to produce 150 bp paired-end reads. Raw reads in fastq format were processed with Fastp (v0.20.1) to remove low-quality sequences and generate clean reads. Quality control was further evaluated using RSeQC (v4.0.0). Clean reads were aligned to the mouse reference genome with HISAT2 (v2.1.0). Gene expression levels were quantified as FPKM, and gene counts were obtained with HTSeq-count (v0.11.2). Differential expression analysis was performed using DESeq2 (v1.20.0), with differentially expressed genes (DEGs) defined as those with $Q < 0.05$ and $|\log_2^{\text{fold change}}| > 1$. The Benjamini–Hochberg procedure was applied to adjust for multiple testing, and Q values were used to control the false discovery rate. Hierarchical clustering of DEGs was performed in R (v3.2.0) to visualize expression profiles. Gene Set Enrichment Analysis (GSEA) was conducted using GSEA software, ranking genes by differential expression and testing enrichment of predefined sets. Significance for GSEA was set at nominal $P < 0.05$ and FDR < 0.25. Functional enrichment analyses, including Gene Ontology (GO) and Kyoto Encyclopedia of Genes and Genomes (KEGG) pathways, were carried out with clusterProfiler (v4.6.0) in R, with adjusted $P < 0.05$ considered significant.

Statistical analysis

For quantitative analysis, the replicates were indicated in the corresponding figure legends. Statistical analysis was performed with GraphPad Prism v9.3.1. and Microsoft Excel 2021. The version of ImageJ software used is Fiji 15.4d. The results are expressed as mean ± s.d. Data were analysed by unpaired two-sided t-test, one-way analysis of variance (ANOVA) with Tukey's multiple comparison test, two-way ANOVA with Tukey's multiple comparison test. A *P* value <0.05 was considered statistically significant.

Data availability

The main data supporting the findings of this study are available within the Article, Supplementary Information, and the Source Data file. Source data are provided with this paper. The raw transcriptomic data generated in this study have been deposited in the NCBI Gene Expression Omnibus (GEO) under accession code PRJNA1305358. The preliminary single-cell transcriptomic data from clinical tissue samples generated during peer review are not publicly available due to confidentiality agreements and ethical restrictions; access can be obtained by contacting the corresponding author and requires appropriate institutional and ethical approvals. All data underlying this study are available from the corresponding author upon request.

References

1 Ferguson, R. J., Palmer, A. J. R., Taylor, A., Porter, M. L., Malchau, H. & Glyn-Jones, S. Hip replacement. *Lancet* **392**, 1662-1671 (2018).

2 Price, A. J., Alvand, A., Troelsen, A., Katz, J. N., Hooper, G., Gray, A., Carr, A. & Beard, D. Knee replacement. *Lancet* **392**, 1672-1682 (2018).

3 Sloan, M., Premkumar, A. & Sheth, N. P. Projected volume of primary total joint arthroplasty in the U.S., 2014 to 2030. *J. Bone Joint Surg.-Am. Vol.* **100**, 1455-1460 (2018).

4 Liang, H., Li, D., Ji, T., Yang, Y., Tang, X. & Guo, W. Implant survival and complication profiles of endoprostheses for treating tumor around the knee in adults: a systematic review of the literature over the past 30 years. *J. Arthroplasty* **33**, 1275-1287 (2018).

5 Cobelli, N., Scharf, B., Crisi, G. M., Hardin, J. & Santambrogio, L. Mediators of the inflammatory response to joint replacement devices. *Nat. Rev. Rheumatol.* **7**, 600-608 (2011).

6 Ishihara, K. Highly lubricated polymer interfaces for advanced artificial hip joints through biomimetic design. *Polym. J.* **47**, 585-597 (2015).

7 Hodges, N. A., Sussman, E. M. & Stegemann, J. P. Aseptic and septic prosthetic joint loosening: Impact of biomaterial wear on immune cell function, inflammation, and infection. *Biomaterials* **278**, 121127-121136 (2021).

8 Archibeck, M. J., Jacobs, J. J., Roebuck, K. A. & Glant, T. T. The basic science of periprosthetic osteolysis. *J. Bone Joint Surg.-Am. Vol.* **82**, 1478-1489 (2000).

9 Boyer, B., Bordini, B., Caputo, D., Neri, T., Stea, S. & Toni, A. Is cross-linked polyethylene an improvement over conventional ultra-high molecular weight polyethylene in total knee arthroplasty? *J. Arthroplasty* **33**, 908-914 (2018).

10 Rochcongar, G., Buia, G., Bourroux, E., Dunet, J., Chapus, V. & Hulet, C. Creep and wear in vitamin E-infused highly cross-linked polyethylene cups for total hip arthroplasty: a prospective randomized controlled

trial. *J. Bone Joint Surg. Am.* **100**, 107-114 (2018).

11 Spece, H., Schachtner, J. T., MacDonald, D. W., Klein, G. R., Mont, M. A., Lee, G.-C. & Kurtz, S. M. Reasons for revision, oxidation, and damage mechanisms of retrieved vitamin E-stabilized highly crosslinked polyethylene in total knee arthroplasty. *J. Arthroplasty* **34**, 3088-3093 (2019).

12 Moro, T., Ishihara, K., Takatori, Y., Tanaka, S., Kyomoto, M., Hashimoto, M., Ishikura, H., Hidaka, R., Tanaka, T., Kawaguchi, H. & Nakamura, K. Effects of a roughened femoral head and the locus of grafting on the wear resistance of the phospholipid polymer-grafted acetabular liner. *Acta Biomater.* **86**, 338-349 (2019).

13 Jarrett, B. T., Cofske, J., Rosenberg, A. E., Oral, E., Muratoglu, O. & Malchau, H. In vivo biological response to vitamin E and vitamin-E-doped polyethylene. *J. Bone Joint Surg. Am.* **92**, 2672-2681 (2010).

14 Goodman, S. B., Yao, Z., Keeney, M. & Yang, F. The future of biologic coatings for orthopaedic implants. *Biomaterials* **34**, 3174-3183 (2013).

15 Chen, W., Bichara, D. A., Suhardi, J., Sheng, P. & Muratoglu, O. K. Effects of vitamin E-diffused highly cross-linked UHMWPE particles on inflammation, apoptosis and immune response against S. aureus. *Biomaterials* **143**, 46-56 (2017).

16 Dominic, A., Le, N. T. & Takahashi, M. Loop Between NLRP3 Inflammasome and Reactive Oxygen Species. *Antioxid. Redox Signal.* **36**, 784-796 (2022).

17 Sies, H., Belousov, V. V., Chandel, N. S., Davies, M. J., Jones, D. P., Mann, G. E., Murphy, M. P., Yamamoto, M. & Winterbourn, C. Defining roles of specific reactive oxygen species (ROS) in cell biology and physiology. *Nat. Rev. Mol. Cell Biol.* **23**, 499-515 (2022).

18 Li, S. F., Dong, C. L., Yuan, C. Q., Liu, S. T. & Bai, X. Q. Effects of CeO_2 nano-particles on anti-aging performance of HDPE polymer during friction. *Wear* **477**, 203832-203840 (2021).

19 Bailey, E. J. & Winey, K. I. Dynamics of polymer segments, polymer chains, and nanoparticles in polymer nanocomposite melts: A review. *Prog. Polym. Sci.* **105**, 101242-101268 (2020).

20 Koo, S., Sohn, H. S., Kim, T. H., Yang, S., Jang, S. Y., Ye, S., Choi, B., Kim, S. H., Park, K. S., Shin, H. M., Park, O. K., Kim, C., Kang, M., Soh, M., Yoo, J., Kim, D., Lee, N., Kim, B.-S., Jung, Y. & Hyeon, T. Ceria-vesicle nanohybrid therapeutic for modulation of innate and adaptive immunity in a collagen-induced arthritis model. *Nat. Nanotechnol.* **18**, 1502-1514 (2023).

21 Kim, Y. G., Lee, Y., Lee, N., Soh, M., Kim, D. & Hyeon, T. Ceria-based therapeutic antioxidants for biomedical applications. *Adv. Mater.* **36**, 2210819 (2024).

22 Sheng, J., Wu, Y., Ding, H., Feng, K., Shen, Y., Zhang, Y. & Gu, N. Multienzyme-like nanozymes: regulation, rational design, and application. *Adv. Mater.* **36**, 2211210 (2024).

23 Ushakov, N. M., Yurkov, G. Y., Gorobinskii, L. V., Popkov, O. V. & Kosobudskii, I. D. Nanocomposites based on the cerium oxide nanoparticles and polyethylene matrix: Syntheses and properties. *Acta Mater.* **56**, 2336-2343 (2008).

24 Gao, W., Xia, Z., Cao, F., Ho, J. C., Jiang, Z. & Qu, Y. Comprehensive understanding of the spatial configurations of CeO_2 in NiO for the electrocatalytic oxygen evolution reaction: embedded or surface-loaded. *Adv. Funct. Mater.* **28**, 1706056 (2018).

25 Zhang, Y., Jing, Z., Jiang, G., Kong, F., Wu, X., Bao, Y., Cui, S. & Shen, Y. A novel PDA/POSS transition layer on the surface of UHMWPE fibers by co-depositing to improve the mechanical properties of composites. *Polymer* **316**, 127856 (2025).

26 Soh, M., Kang, D. W., Jeong, H. G., Kim, D., Kim, D. Y., Yang, W., Song, C., Baik, S., Choi, I. Y., Ki, S. K., Kwon, H. J., Kim, T., Kim, C. K., Lee, S. H. & Hyeon, T. Ceria-Zirconia Nanoparticles as an Enhanced Multi-Antioxidant for Sepsis Treatment. *Angew. Chem. Int. Edit.* **56**, 11399-11403 (2017).

27 Oral, E., Ghali, B. W., Neils, A. & Muratoglu, O. K. A new mechanism of oxidation in ultrahigh molecular weight polyethylene caused by squalene absorption. *J. Biomed. Mater. Res. B* **100**, 742-751 (2012).

28 Bracco, P., Costa, L., Luda, M. P. & Billingham, N. A review of experimental studies of the role of free-radicals in polyethylene oxidation. *Polym. Degrad. Stabil.* **155**, 67-83 (2018).

29 Collier, J. P., Currier, B. H., Kennedy, F. E., Currier, J. H., Timmins, G. S., Jackson, S. K. & Brewer, R. L. Comparison of cross-linked polyethylene materials for orthopaedic applications. *Clin. Orthop. Relat. R.* **414**, 289-304 (2003).

30 Dasari, A., Yu, Z.-Z. & Mai, Y.-W. Fundamental aspects and recent progress on wear/scratch damage in polymer nanocomposites. *Mat. Sci. Eng. R* **63**, 31-80 (2009).

31 Fu, S.-Y., Feng, X.-Q., Lauke, B. & Mai, Y.-W. Effects of particle size, particle/matrix interface adhesion and particle loading on mechanical properties of particulate-polymer composites. *Compos. Part B-Eng.* **39**, 933-961 (2008).

32 Che, J., Wu, K., Lin, Y., Wang, K. & Fu, Q. Largely improved thermal conductivity of HDPE/expanded graphite/carbon nanotubes ternary composites via filler network-network synergy. *Compos. Part A-Appl. Sci.* **99**, 32-40 (2017).

33 Johnsen, B. B., Kinloch, A. J., Mohammed, R. D., Taylor, A. C. & Sprenger, S. Toughening mechanisms of nanoparticle-modified epoxy polymers. *Polymer* **48**, 530-541 (2007).

34 Haidar, D. R., Ye, J., Moore, A. C. & Burris, D. L. Assessing quantitative metrics of transfer film quality as indicators of polymer wear performance. *Wear* **380-381**, 78-85 (2017).

35 Dickinson, B. C. & Chang, C. J. Chemistry and biology of reactive oxygen species in signaling or stress responses. *Nat. Chem. Biol.* **7**, 504-511 (2011).

36 Green, T. R., Fisher, J., Stone, M., Wroblewski, B. M. & Ingham, E. Polyethylene particles of a 'critical size' are necessary for the induction of cytokines by macrophages in vitro. *Biomaterials* **19**, 2297-2302 (1998).

37 Forman, H. J. & Zhang, H. Targeting oxidative stress in disease: promise and limitations of antioxidant therapy. *Nat. Rev. Drug Discov.* **20**, 689-709 (2021).

38 Liu, Y., Shi, F., Bo, L., Zhi, W., Weng, J. & Qu, S. A novel alginate-encapsulated system to study biological response to critical-sized wear particles of UHMWPE loaded with alendronate sodium. *Mater. Sci. Eng. C-Mater. Biol. Appl.* **79**, 679-686 (2017).

39 Cordova, L. A., Stresing, V., Gobin, B., Rosset, P., Passuti, N., Gouin, F., Trichet, V., Layrolle, P. & Heymann, D. Orthopaedic implant failure: aseptic implant loosening-the contribution and future challenges of mouse models in translational research. *Clin Sci* **127**, 277-293 (2014).

40 Bayliss, L. E., Culliford, D., Monk, A. P., Glyn-Jones, S., Prieto-Alhambra, D., Judge, A., Cooper, C., Carr, A. J., Arden, N. K. & Beard, D. J. The effect of patient age at intervention on risk of implant revision after total replacement of the hip or knee: a population-based cohort study. *Lancet* **389**, 1424-1430 (2017).

41 Dutta, S. & Sengupta, P. Men and mice: relating their ages. *Life Sci.* **152**, 244-248 (2016).

42 Liu, X., Wu, J., Liu, Q., Lin, A., Li, S., Zhang, Y., Wang, Q., Li, T., An, X., Zhou, Z., Yang, M. & Wei, H. Synthesis-temperature-regulated multi-enzyme-mimicking activities of ceria nanozymes. *J Mater Chem B* **9**, 7238-7245 (2021).

43 Li, C., Guo, C., Fitzpatrick, V., Ibrahim, A., Zwierstra, M. J., Hanna, P., Lechtig, A., Nazarian, A., Lin, S. J. & Kaplan, D. L. Design of biodegradable, implantable devices towards clinical translation. *Nat. Rev. Mater.* **5**, 61-81 (2019).

44 Chung, L., Maestas, D. R., Lebid, A., Mageau, A., Rosson, G. D., Wu, X., Wolf, M. T., Tam, A. J., Vanderzee, I., Wang, X., Andorko, J. I., Zhang, H., Narain, R., Sadtler, K., Fan, H., Čiháková, D., Le Saux, C. J., Housseau, F., Pardoll, D. M. & Elisseeff, J. H. Interleukin 17 and senescent cells regulate the foreign body response to synthetic material implants in mice and humans. *Sci. Transl. Med.* **12**, eaax3799 (2020).

45 Theocharidis, G., Yuk, H., Roh, H., Wang, L., Mezghani, I., Wu, J., Kafanas, A., Contreras, M., Sumpio, B., Li, Z., Wang, E., Chen, L., Guo, C. F., Jayaswal, N., Katopodi, X.-L., Kalavros, N., Nabzdyk, C. S., Vlachos, I. S., Veves, A. & Zhao, X. A strain-programmed patch for the healing of diabetic wounds. *Nat. Biomed. Eng.* **6**, 1118-1133 (2022).

46 Dellacherie, M. O., Seo, B. R. & Mooney, D. J. Macroscale biomaterials strategies for local immunomodulation. *Nat. Rev. Mater.* **4**, 379-397 (2019).

47 Cronk, J. C., Derecki, N. C., Ji, E., Xu, Y., Lampano, A. E., Smirnov, I., Baker, W., Norris, G. T., Marin, I., Coddington, N., Wolf, Y., Turner, S. D., Aderem, A., Klibanov, A. L., Harris, T. H., Jung, S., Litvak, V. & Kipnis, J. Methyl-CpG binding protein 2 regulates microglia and macrophage gene expression in response to inflammatory stimuli. *Immunity* **42**, 679-691 (2015).

48 Novershtern, N., Subramanian, A., Lawton, L. N., Mak, R. H., Haining, W. N., McConkey, M. E., Habib, N., Yosef, N., Chang, C. Y., Shay, T., Frampton, G. M., Drake, A. C., Leskov, I., Nilsson, B., Preffer, F., Dombkowski, D., Evans, J. W., Liefeld, T., Smutko, J. S., Chen, J., Friedman, N., Young, R. A., Golub, T. R., Regev, A. & Ebert, B. L. Densely interconnected transcriptional circuits control cell states in human hematopoiesis. *Cell* **144**, 296-309 (2011).

49 Ganz, T. Anemia of inflammation. *N. Engl. J. Med.* **381**, 1148-1157 (2019).

50 Oh, J. E., Iijima, N., Song, E., Lu, P., Klein, J., Jiang, R., Kleinstein, S. H. & Iwasaki, A. Migrant memory B cells secrete luminal antibody in the vagina. *Nature* **571**, 122-126 (2019).

51 Santambrogio, L. & Marrack, P. The broad spectrum of pathogenic autoreactivity. *Nat. Rev. Immunol.* **23**, 69-70 (2023).

52 Kurien, B. T., Hensley, K., Bachmann, M. & Scofield, R. H. Oxidatively modified autoantigens in autoimmune diseases. *Free Radical Bio. Med.* **41**, 549-556 (2006).

53 Shapiro-Shelef, M. & Calame, K. Regulation of plasma-cell development. *Nat. Rev. Immunol.* **5**, 230-242 (2005).

54 Chu, V. T. & Berek, C. The establishment of the plasma cell survival niche in the bone marrow. *Immunol. Rev.* **251**, 177-188 (2012).

55 Kunkel, E. J. & Butcher, E. C. Plasma-cell homing. *Nat. Rev. Immunol.* **3**, 822-829 (2003).

56 Walsh, M. C., Takegahara, N., Kim, H. & Choi, Y. Updating osteoimmunology: regulation of bone cells by innate and adaptive immunity. *Nat. Rev. Rheumatol.* **14**, 146-156 (2018).

57 Grcevic, D., Sanjay, A. & Lorenzo, J. Interactions of B-lymphocytes and bone cells in health and disease. *Bone* **168**, 116296 (2023).

58 Weitzmann, M. N. & Ofotokun, I. Physiological and pathophysiological bone turnover - role of the immune system. *Nat. Rev. Endocrinol.* **12**, 518-532 (2016).

59 van de Donk, N. W. C. J., Pawlyn, C. & Yong, K. L. Multiple myeloma. *Lancet* **397**, 410-427 (2021).

60 Kristyanto, H., Blomberg, N. J., Slot, L. M., van der Voort, E. I. H., Kerkman, P. F., Bakker, A., Burgers, L. E., ten Brinck, R. M., van der Helm-van Mil, A. H. M., Spits, H., Baeten, D. L., Huizinga, T. W. J., Toes, R. E. M. & Scherer, H. U. Persistently activated, proliferative memory autoreactive B cells promote inflammation in rheumatoid arthritis. *Sci. Transl. Med.* **12**, eaaz5327 (2020).

61 Rajakumar, S. A., Papp, E., Lee, K. K., Grandal, I., Merico, D., Liu, C. C., Allo, B., Zhang, L., Grynpas, M. D., Minden, M. D., Hitzler, J. K., Guidos, C. J. & Danska, J. S. B cell acute lymphoblastic leukemia cells mediate RANK-RANKL–dependent bone destruction. *Sci. Transl. Med.* **12**, eaba5942 (2020).

62 Moore, E. M., Maestas Jr, D. R., Cherry, C. C., Garcia, J. A., Comeau, H. Y., Davenport Huyer, L., Kelly, S. H., Peña, A. N., Blosser, R. L. & Rosson, G. D. Biomaterials direct functional B cell response in a material-specific manner. *Sci. Adv.* **7**, eabj5830 (2021).

63 Doloff, J. C., Veiseh, O., Vegas, A. J., Tam, H. H., Farah, S., Ma, M., Li, J., Bader, A., Chiu, A., Sadraei, A., Aresta-Dasilva, S., Griffin, M., Jhunjhunwala, S., Webber, M., Siebert, S., Tang, K., Chen, M., Langan, E., Dholokia, N., Thakrar, R., Qi, M., Oberholzer, J., Greiner, D. L., Langer, R. & Anderson, D. G. Colony stimulating factor-1 receptor is a central component of the foreign body response to biomaterial implants in rodents and non-human primates. *Nat. Mater.* **16**, 671-680 (2017).

64 Doloff, J. C., Veiseh, O., de Mezerville, R., Sforza, M., Perry, T. A., Haupt, J., Jamiel, M., Chambers, C., Nash, A., Aghlara-Fotovat, S., Stelzel, J. L., Bauer, S. J., Neshat, S. Y., Hancock, J., Romero, N. A., Hidalgo, Y. E., Leiva, I. M., Munhoz, A. M., Bayat, A., Kinney, B. M., Hodges, H. C., Miranda, R. N., Clemens, M. W. & Langer, R. The surface topography of silicone breast implants mediates the foreign body response in mice, rabbits and humans. *Nat. Biomed. Eng.* **5**, 1115-1130 (2021).

65 Higgins, D. M., Basaraba, R. J., Hohnbaum, A. C., Lee, E. J., Grainger, D. W. & Gonzalez-Juarrero, M. Localized immunosuppressive environment in the foreign body response to implanted biomaterials. *Am. J. Pathol.* **175**, 161-170 (2009).

66 Paton-Hough, J., Chantry, A. D. & Lawson, M. A. A review of current murine models of multiple myeloma used to assess the efficacy of therapeutic agents on tumour growth and bone disease. *Bone* **77**, 57-68 (2015).

67 Manasanch, E. E. & Orlowski, R. Z. Proteasome inhibitors in cancer therapy. *Nat. Rev. Clin. Oncol.* **14**, 417-433 (2017).

68 Abu-Amer, Y., Darwech, I. & Clohisy, J. C. Aseptic loosening of total joint replacements: mechanisms underlying osteolysis and potential therapies. *Arthrit. Res. Ther.* **9**, S6 (2007).

69 Thillemann, T. M., Pedersen, A. B., Mehnert, F., Johnsen, S. P. & Søballe, K. Postoperative use of bisphosphonates and risk of revision after primary total hip arthroplasty: A nationwide population-based study. *Bone* **46**, 946-951 (2010).

70 Griffin, D. R., Archang, M. M., Kuan, C. H., Weaver, W. M., Weinstein, J. S., Feng, A. C., Ruccia, A., Sideris, E., Ragkousis, V., Koh, J., Plikus, M. V., Di Carlo, D., Segura, T. & Scumpia, P. O. Activating an adaptive immune response from a hydrogel scaffold imparts regenerative wound healing. *Nat. Mater.* **20**, 560-569 (2021).

71 Li, X., Gong, N., Tian, F., Zhang, S., Zhang, Y., Wang, Y., Qing, G., Wang, Y., Li, F., Xu, Y., Zhang, L., Wang, J., Ni, Q., Gan, Y., Gu, C., Jiang, H., Huang, X., Shi, X., Zhang, T., Wu, Y. & Liang, X.-J. Suppression of cytokine release syndrome during CAR-T-cell therapy via a subcutaneously injected interleukin-6-adsorbing hydrogel. *Nat. Biomed. Eng.* **7**, 1129-1141 (2023).

72 Kurien, B. T. & Scofield, R. H. Autoimmunity and oxidatively modified autoantigens. *Autoimmun. Rev* **7**,

567-573 (2008).

73 Noack, M. & Miossec, P. Importance of lymphocyte-stromal cell interactions in autoimmune and inflammatory rheumatic diseases. *Nat. Rev. Rheumatol.* **17**, 550-564 (2021).

74 Nabiyev, A. A., Olejniczak, A., Pawlukojc, A., Balasoiu, M., Bunoiu, M., Maharramov, A. M., Nuriyev, M. A., Ismayilova, R. S., Azhibekov, A. K., Kabyshev, A. M., Ivankov, O. I., Vlase, T., Linnik, D. S., Shukurova, A. A., Ivanshina, O. Y., Turchenko, V. A. & Kuklin, A. I. Nano-ZrO_2 filled high-density polyethylene composites: Structure, thermal properties, and the influence γ-irradiation. *Polym. Degrad. Stabil.* **171**, 109042 (2020).

75 *Plastics - Determination of tensile properties*, ISO 527 (International Organization for Standardization, 2021).

76 *Standard Test Methods for Determining the Izod Pendulum Impact Resistance of Plastics*, ASTM D256-18 (American Society for Testing Materials, 2018).

77 Llorente, J., Román-Manso, B., Miranzo, P. & Belmonte, M. Tribological performance under dry sliding conditions of graphene/silicon carbide composites. *J. Eur. Ceram. Soc.* **36**, 429-435 (2016).

78 *Standard Test Method for Linearly Reciprocating Ball-on-Flat Sliding Wear*, ASTM G133-10 (American Society for Testing Materials, 2010).

79 *Standard Guide for Accelerated Aging of Sterile Barrier Systems for Medical Devices*, ASTM F1980-16 (American Society for Testing Materials, 2016).

80 *Standard Guide for Evaluating the Extent of Oxidation in Polyethylene Fabricated Forms Intended for Surgical Implants*, ASTM F2102-17 (American Society for Testing Materials, 2017).

81 Baxter, R. M., MacDonald, D. W., Kurtz, S. M. & Steinbeck, M. J. Characteristics of highly cross-linked polyethylene wear debris in vivo. *J. Biomed. Mater. Res. Part B* **101**, 467-475 (2013).

82 Yang, Z., Luo, S., Zeng, Y., Shi, C. & Li, R. Albumin-mediated biomineralization of shape-controllable and biocompatible ceria nanomaterials. *ACS Appl. Mater. Interfaces* **9**, 6839-6848 (2017).

83 Dempster, D. W., Compston, J. E., Drezner, M. K., Glorieux, F. H., Kanis, J. A., Malluche, H., Meunier, P. J., Ott, S. M., Recker, R. R. & Parfitt, A. M. Standardized nomenclature, symbols, and units for bone histomorphometry: a 2012 update of the report of the ASBMR Histomorphometry Nomenclature Committee. *J. Bone Miner. Res.* **28**, 2-17 (2013).

84 Shea, K. G., Bloebaum, R. D., Avent, J. M., Birk, G. T. & Samuelson, K. M. Analysis of lymph nodes for polyethylene particles in patients who have had a primary joint replacement. *The Journal of Bone & Joint Surgery* **78**, 497-504 (1996).

Acknowledgments

We thank Ms. Yan Yuan and Ms. Dandan Xu from Environment and Renewable Energy Testing Center of Nanjing University for providing invaluable assistance with the DSC analysis. We thank Dr. Quan Wang for help in SOD-like activity and •OH scavenging activity tests. We thank Ms. Hanjie Zhang and Mr. Dongze Mo for help in animal models. We thank Dr. Deku Zhang and Mr. Lian Zhang for the assistance in polymer molding. We thank Prof. Xiaoniu Yang, Prof. Guanghao

Lu, Dr. Fushi Li, Mr. Wei Bao, and Mr. Lingfeng Hu for the assistance in mechanical testing. We thank Ms. Yuting Wang for the valuable advice in the schematic illustration. The writing has been refined with the assistance of DeepSeek and OpenAI.

Funding

H.W. discloses support for the research of this work from the Jiangsu Provincial Key R&D Program [BE2022836], the National Natural Science Foundation of China [22374071], the State Key Laboratory of Analytical Chemistry for Life Science [5431ZZXM2501], the Fundamental Research Funds for the Central Universities [2025300292], the opening foundation of the NMPA Key Laboratory for Biomedical Optics [20240001], the PAPD Program, the Key Program of Nanozyme Laboratory in Zhongyuan, and the International Expansion and Enhancement Program by Nanjing University International Affairs Office. Q.J. discloses support for the research of this work from the National Natural Science Foundation of China [92368201] and the Shenzhen Medical Research Fund [B2302005]. X.R. discloses support for the research of this work from the Natural Science Foundation of Jiangsu Province [BK20232017]. L.Z. discloses support for the research of this work from the National Natural Science Foundation of China [32401092] and the China Postdoctoral Science Foundation [2022M722769, 2024T170775].

Author Contributions Statement

H.W., Q.J., and L.Z. conceived and supervised the project. S.L. and L.Z. designed and performed the majority of experiments, analysed the data and wrote the manuscript. S.Z. and Y.L. helped in conceptualization of idea. Q.S., Q.L., Y.Z., L.J., T.L., J.C., J.W., J.Z. (Jingyuan Zhao) and X.C. assisted with experiments and discussion. J.Z. (Jingjing Zhang), X.R., and Y.D. revised the final manuscript. All authors discussed and commented on the manuscript.

Corresponding authors

Correspondence to Liming Zheng, Qing Jiang, and Hui Wei.

Competing Interests Statement

H.W., S.L., and L.Z. are inventors on a granted patent (CN116942900B) related to the design and application of prosthetic materials described in this manuscript. The patent applicant is Nanjing University. All other authors declare no competing interests.

Figure Legends

Fig. 1: Illustration of the proactive preventive strategy employing CZPE as a model system. **a**, Scheme of synthesis and mechanical shaping of CZPE for knee joint liners (Created in BioRender. Liu, S. (2025) https://BioRender.com/vghjnq7). Step 1: dissolution of UHMWPE to obtain a homogeneous system for uniformly dispersed polymer; Step 2: introduction of cerium acetylacetonate, ensuring uniform dispersion of the metal-organic precursor within the polymer solution; Step 3: crystallization and formation of CeO_2 NPs; Step 4: cleaning and mechanical processing to thermocompress and machine the amorphous CZPE material into specific shapes. **b**, Scheme of the prevention effect of CZPE on WPO. Under mechanical loading, CZPE bulk material exhibits a lower incidence of wear particle generation compared to its PE counterpart. Subsequent to generation, CZPE particles induce lower levels of ROS production by macrophages relative to PE particles. This reduction in ROS stimulation contributes to the alleviation of chronic inflammation, osteolysis and FBR. Furthermore, CZPE particles mitigate intramedullary plasma cell infiltration compared to PE particles, contributing to reduced bone resorption.

Fig. 2: Characterizations of CZPE bulk samples. a, XRD patterns of UHMWPE and CZPE before and after hot pressing. **b**, Scheme of oxidative aging treatment. **c**, FT-IR spectra of CZPE-1, CZPE-5, CZPE-10, and PE bulk samples after four months of aging treatment. **d**, Relative oxidation indices of CZPE-1, CZPE-5, CZPE-10, and PE bulk samples after four months of aging (n = 6 independent specimens per group). **e**, Scheme of tensile testing. **f**, Ultimate tensile strength of CZPE-1, CZPE-5, CZPE-10, and PE bulk samples (n = 5 independent specimens per group). Dotted line indicates the minimum value of clinically used UHMWPE[29]. **g**, Scheme of notched Izod impact testing. **h**, Impact strengths of CZPE-1, CZPE-5, CZPE-10, and PE bulk samples (n = 5 independent specimens per group). Dotted line indicates the minimum value of clinically used

UHMWPE[29]. **i**, Scheme of friction testing. **j**, Wear rates of CZPE-1, CZPE-5, CZPE-10, and PE bulk samples (n = 6 independent specimens per group). Data in **d, f, h, and j** are presented as mean ± standard deviation (s. d.). P values in **d, f, and h** and were analysed by one-way analysis of variance (ANOVA) with Tukey's multiple comparisons test. P values in **j** were analysed by one-way ANOVA with Dunnett's test against the PE group. NS, not significant, $P \geq 0.05$. Source data are provided as a Source Data file.

Fig. 3: Reduced inflammatory and osteoclastogenic effects of CZPE-5 particles. a, Illustration of depicting the mechanism underlying the SOD- and CAT-like activities of CZPE-5 particles in scavenging $O_2^{\bullet-}$ and H_2O_2. **b**, **c**, Antioxidative activity assays comparing CZPE-5 and PE particles: SOD-like activity (**b**) and CAT-like activity (**c**) (n = 3 independent specimens per group). **d**, **e**, Assays evaluating the antioxidative activities of CZPE-5 and PE particles post one-year immersion in PBS: SOD-like activity (**d**) and CAT-like activity (**e**) (n = 3 independent specimens per group). **f**, **g**, Measurements (**f**) and quantifications (**g**) of ROS expression in RAW264.7 cells as analysed by flow cytometry (n = 4 biological replicates per group). **h-j**, Relative mRNA expression levels of *Il6* (**h**), *Il1b* (**i**), and *Tnf* (**j**) in RAW264.7 cells stimulated by wear particles (n = 3 biological replicates per group). **k-m**, Relative mRNA expression levels of *IL6* (**k**), *IL1B* (**l**), and *TNF* (**m**) in THP-1-derived macrophages stimulated by wear particles (n = 3 biological replicates per group). **n**, Representative TRAP staining images of osteoclast. Scale bar, 200 μm. **o**, Corresponding quantification of osteoclast areas (n = 5 biological replicates per group). For **n** and **o**, the Ctrl group refers to cells cultured in osteoclast medium. **p**, Schematic representation and timeline of the particle-induced cranial defect model (Created in BioRender. Liu, S. (2025) https://BioRender.com/sm1zqgs). **q**, Representative micro-CT images of calvarial bones at day 14 post-injection. Scale bar, 1 mm. **r**, Quantifications of relative BV/TV based on micro-CT (n = 5 biological replicates per group). **s**, Representative histological images of bone sections stained with TRAP at day 14 post-injection. Top: 20× magnification, scale bar, 100 μm; Bottom: 80× magnification, scale bar, 25 μm. **t**, Quantifications of %E. Pm based on TRAP-stained sections (n = 5 biological replicates per group). Data in **b-e, g, h-m, o, r, t** are presented as mean ± s.d. P values for **b-e, g** were analysed by an unpaired two-sided t-test, while for **h-m, o, r, t** were analysed by one-way ANOVA with Tukey's multiple comparisons test. NS, not significant, $P \geq 0.05$. Although the individual values of the Ctrl and CZPE groups in **k** and **m** do not overlap, the statistical analysis does not indicate a significant difference, likely due to the limited sample size. Source data

are provided as a Source Data file.

Fig. 4: Reduced WPO-inducing potential of CZPE particles. **a**, Schematic illustration and timeline of the distal femoral implant model (Created in BioRender. Liu, S. (2025) https://BioRender.com/wmu80el). **b**, Representative micro-CT images of the femoral transverse section at day 49 post-injection. Main images: femoral cross-section parallel to the direction of nail insertion. Insets: femoral cross-section perpendicular to the direction of nail insertion. Scale bar, 1 mm. **c**, Quantifications of relative BV/TV based on micro-CT (n = 5 biological replicates per group). **d**, Representative histological images of TRAP-stained bone sections at day 49 post-surgery. Left: 3× magnification, scale bar, 500 μm; Right: 48× magnification, scale bar, 50 μm. **e**, Quantifications of %E. Pm based on TRAP-stained sections (n = 5 biological replicates per group). **f**, Representative immunofluorescence staining of femoral sections from experimental mice at day 49 post-surgery. Green indicates IL-1β; blue indicates DAPI nuclear stain. Scale bar, 200 μm. **g**, Intensity quantification of IL-1β immunofluorescence staining (n = 4 biological replicates per group). **h**, Representative histochemical images of femoral sections stained with Masson's trichrome for collagen at day 49 post-surgery, showcasing areas with the most severe foreign body reactions across all groups. The areas of fibrotic capsules were marked with black line segments. Scale bar, 100 μm. **i**, Fiber capsule thickness determined by measuring collagen thickness surrounding the titanium alloy nails using Masson's trichrome staining (n = 30 measurements per group, derived from 5 biological replicates, 6 measurements per sample). **j**, Representative immunofluorescence images for DAPI and α-SMA co-staining. Green indicates α-SMA; blue indicates DAPI nuclear stain. Scale bar, 20 μm. **k,** The quantification of α-SMA$^+$ cells per unit area (n = 5 biological replicates per group). The Ctrl group refers to mice subjected to the same surgical procedure but injected with FBS only. Data in **c, e, g, i,** and **k** are presented as mean ± s.d. P values for **c, e, g, i** and **k** were analysed by one-way ANOVA with Tukey's multiple comparisons test. NS, not significant, $P \geq 0.05$. Asterisk denotes titanium alloy bone nail. Source data are provided as a Source Data file.

Fig. 5: Preventive effect of CZPE on WPO associated with plasma cell-mediated pathway. **a**, Heat map of differentially expressed mRNAs ($q < 0.05$, $|\log_2^{\text{fold change}}| > 1$) related to plasma cell marker, transcription factors, and transcriptional coactivators. **b**, Immunofluorescence of femoral sections at day 49 post-

surgery. Green, CD138; red, B220; blue, DAPI. Scale bar, 30 μm. **c**, Density of $CD138^{+}/B220^{-}$ cells (n = 4 biological replicates per group). **d**, Relative *Sdc1* mRNA expression (n = 3 biological replicates per group). **e**, Western blot analysis of CD138. β-Actin as loading control. **f**, Quantified protein levels (n = 3 biological replicates per group), all from the same experiment, processed in parallel. **g**, Timeline for distal femoral implant model with U266B1 cells injection. **h**, Micro-CT images of femoral cross-sections from U266B1 cells injected mice; main, parallel; inset, perpendicular to nail insertion. Scale bar, 1 mm. **i**, Relative BV/TV (n = 6 biological replicates per group). **j**, TRAP-stained bone sections from U266B1-injected mice. Top: 16× magnification, scale bar, 100 μm; Bottom: 64× magnification, scale bar, 25 μm. **k**, %E. Pm from TRAP-stained sections (n = 6 biological replicates per group). **l**, Timeline for bortezomib administration. **m**, Micro-CT images after bortezomib treatment, as in **h**. **n**, Relative BV/TV (n = 6 biological replicates per group). **o**, TRAP-stained bone sections from bortezomib-treated mice, as in **j**. **p**, %E. Pm from TRAP-stained sections (n = 6 biological replicates per group). For **a**–**f**, the Ctrl group refers to mice that underwent same surgical procedure with FBS injection only. For **h**–**k** and **m**–**p**, the Ctrl-PBS, Ctrl-U266B1, and Ctrl-Bortezomib groups refer to mice that underwent the same surgical procedure with FBS injection only, followed by PBS, U266B1 cells, or bortezomib injection, respectively, four weeks after surgery. Data are presented as mean ± s.d. P values: **c, d, and f** by one-way ANOVA with Tukey's multiple comparisons test; **i**, **k** by an unpaired two-sided t-test; **n, p** by two-way ANOVA with Tukey's multiple comparisons test. NS, not significant, $P \geq 0.05$. Although the individual values of the Ctrl and CZPE groups in **d** and **f** do not overlap, the statistical analysis does not indicate a significant difference, likely due to the limited sample size. Source data are provided as a Source Data file.

Traditional strategies to address wear particle-induced osteolysis largely focus on reducing wear generation, rather than mitigating the immunostimulatory effects elicited by wear particles. Here, the authors report a proactive preventive approach to implant design, that adopts CeO_2 nanozymes-incorporated liners to actively limit the harmful immune effects of particles.

Peer Review Information: *Nature Communications* thanks Xinlin Yang, and the other, anonymous, reviewer(s) for their contribution to the peer review of this work. A peer review file is available.

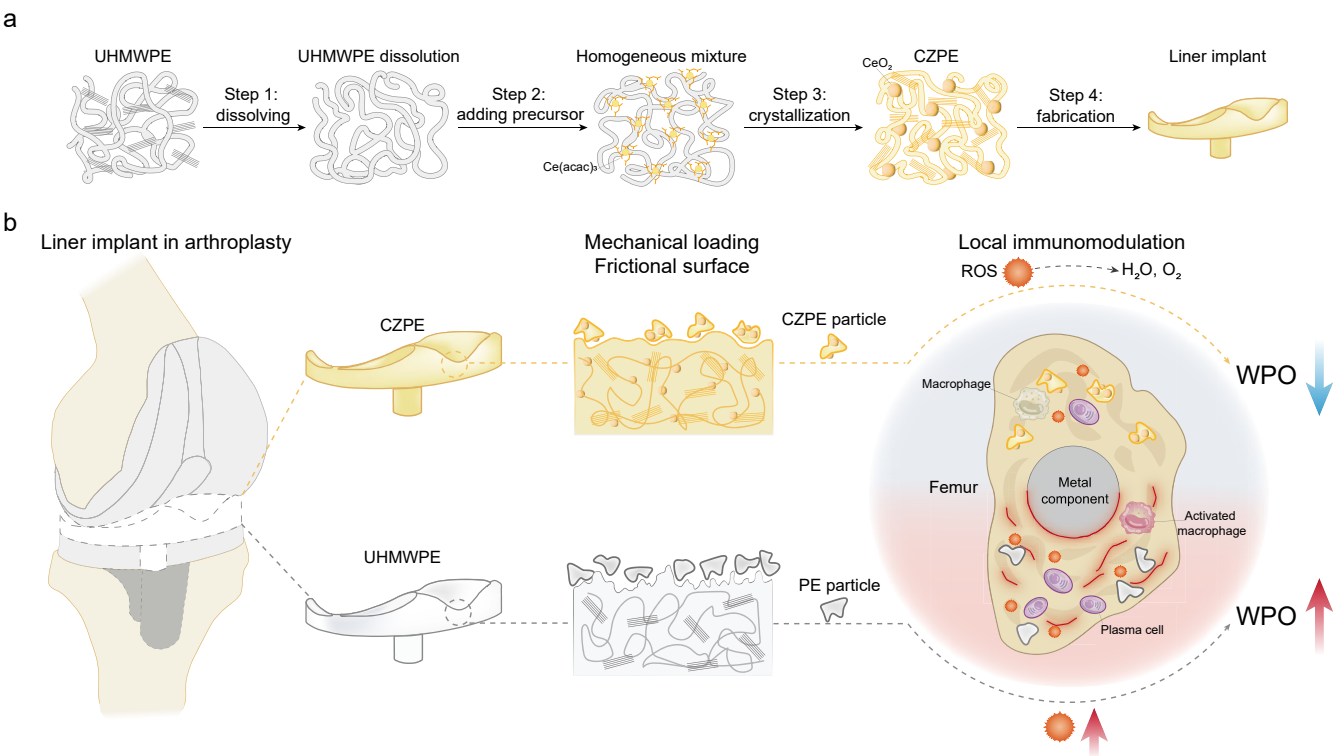
a
UHMWPE
Step 1:
dissolving
UHMWPE dissolution
Step 2:
adding precursor
Homogeneous mixture
Ce(acac)3
Step 3:
crystallization
CeO2
CZPE
Step 4:
fabrication
Liner implant
b
Liner implant in arthroplasty
CZPE
UHMWPE
Mechanical loading
Frictional surface
CZPE particle
PE particle
Local immunomodulation
ROS
H2O, O2
Macrophage
Femur
Metal
component
Activated
macrophage
Plasma cell
WPO
WPO

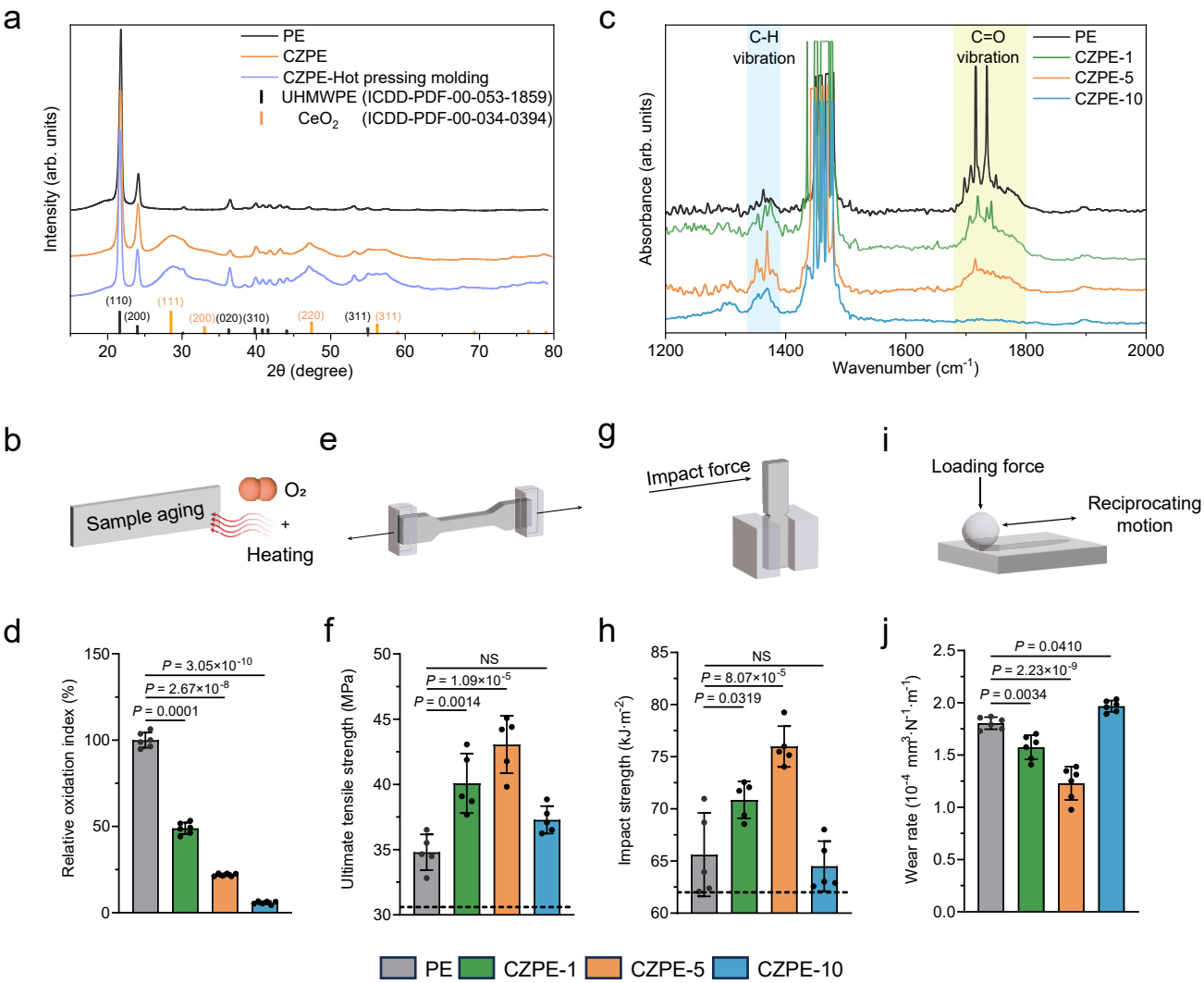
a
PE
CZPE
CZPE-Hot pressing molding
UHMWPE (ICDD-PDF-00-053-1859)
CeO2 (ICDD-PDF-00-034-0394)
Intensity (arb. units)
2θ (degree)
(110)
(200)
(111)
(200)(020)(310)
(220)
(311)
(311)
c
C-H vibration
C=O vibration
PE
CZPE-1
CZPE-5
CZPE-10
Absorbance (arb. units)
Wavenumber (cm-1)
b
Sample aging
O2
+
Heating
e
g
Impact force
i
Loading force
Reciprocating motion
d
Relative oxidation index (%)
P = 3.05×10-10
P = 2.67×10-8
P = 0.0001
f
Ultimate tensile strength (MPa)
NS
P = 1.09×10-5
P = 0.0014
h
Impact strength (kJ·m-2)
NS
P = 8.07×10-5
P = 0.0319
j
Wear rate (10-4 mm3·N-1·m-1)
P = 0.0410
P = 2.23×10-9
P = 0.0034
PE
CZPE-1
CZPE-5
CZPE-10

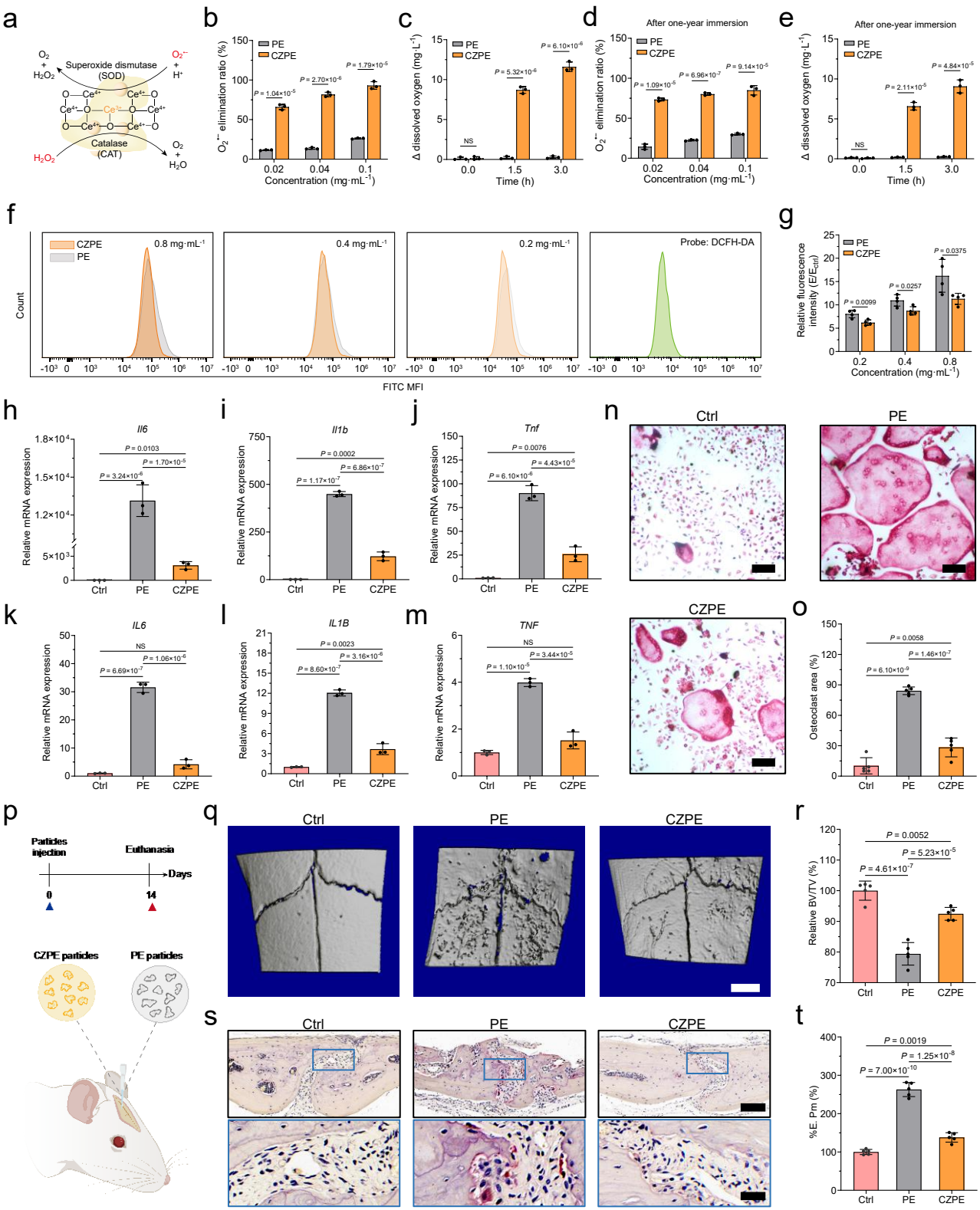
a
b
c
d
e
f
g
h
i
j
n
k
l
m
o
p
q
r
s
t
Superoxide dismutase (SOD)
Catalase (CAT)
PE
CZPE
Concentration (mg·mL-1)
Time (h)
After one-year immersion
Probe: DCFH-DA
FITC MFI
Count
Relative mRNA expression
Relative fluorescence intensity
Osteoclast area (%)
Relative BV/TV (%)
%E. Pm (%)
Ctrl
Il6
Il1b
Tnf
IL6
IL1B
TNF
Particles injection
Euthanasia
Days
CZPE particles
PE particles

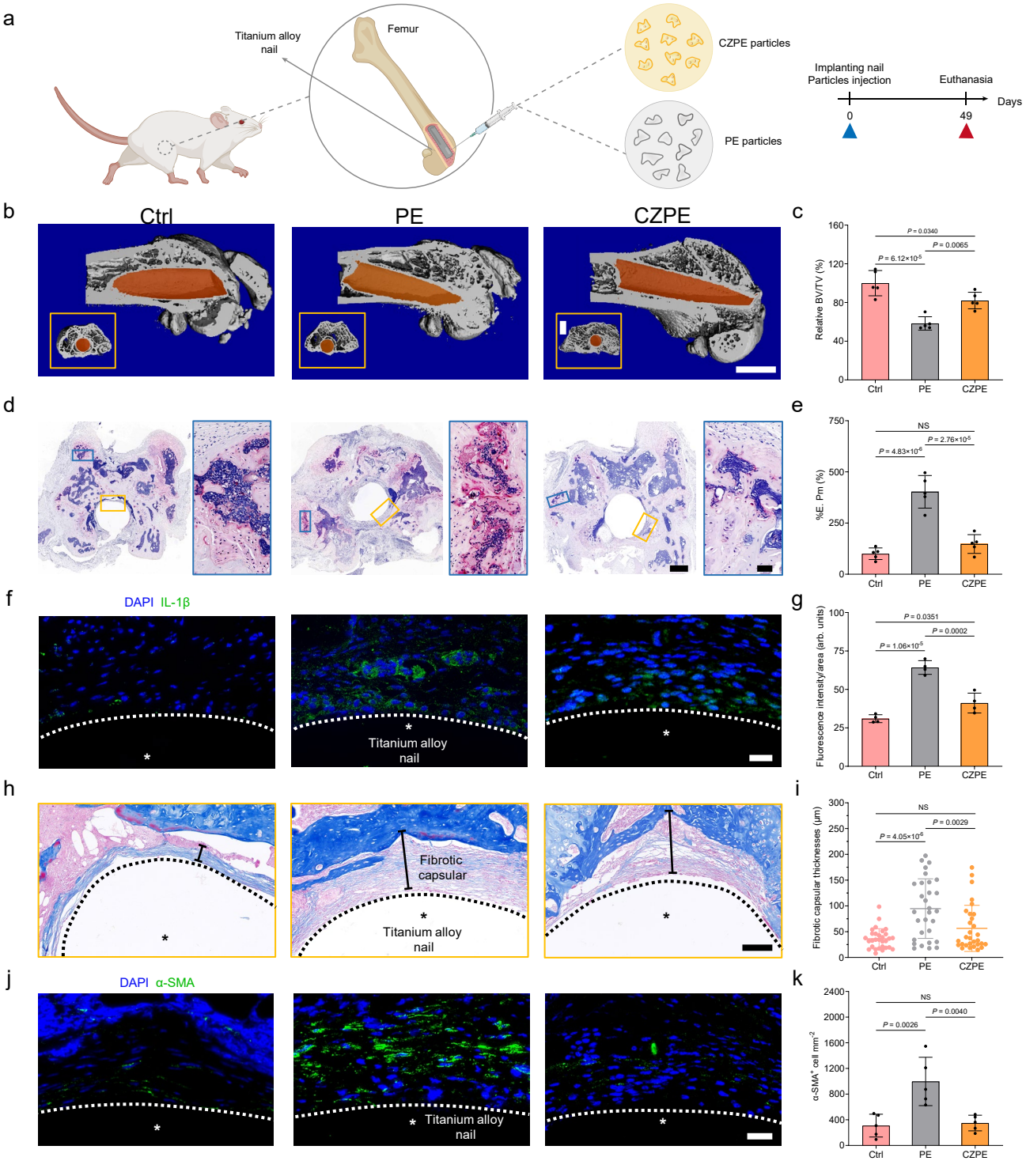
a
Titanium alloy nail
Femur
CZPE particles
PE particles
Implanting nail
Particles injection
Euthanasia
Days
0
49
b
Ctrl
PE
CZPE
c
Relative BV/TV (%)
P = 0.0340
P = 0.0065
P = 6.12×10-5
Ctrl
PE
CZPE
d
e
%E. Pm (%)
NS
P = 2.76×10-5
P = 4.83×10-6
f
DAPI IL-1β
Titanium alloy nail
g
Fluorescence intensity/area (arb. units)
P = 0.0351
P = 0.0002
P = 1.06×10-5
h
Fibrotic capsular
Titanium alloy nail
i
Fibrotic capsular thicknesses (μm)
NS
P = 0.0029
P = 4.05×10-6
j
DAPI α-SMA
Titanium alloy nail
k
α-SMA+ cell mm-2
NS
P = 0.0040
P = 0.0026

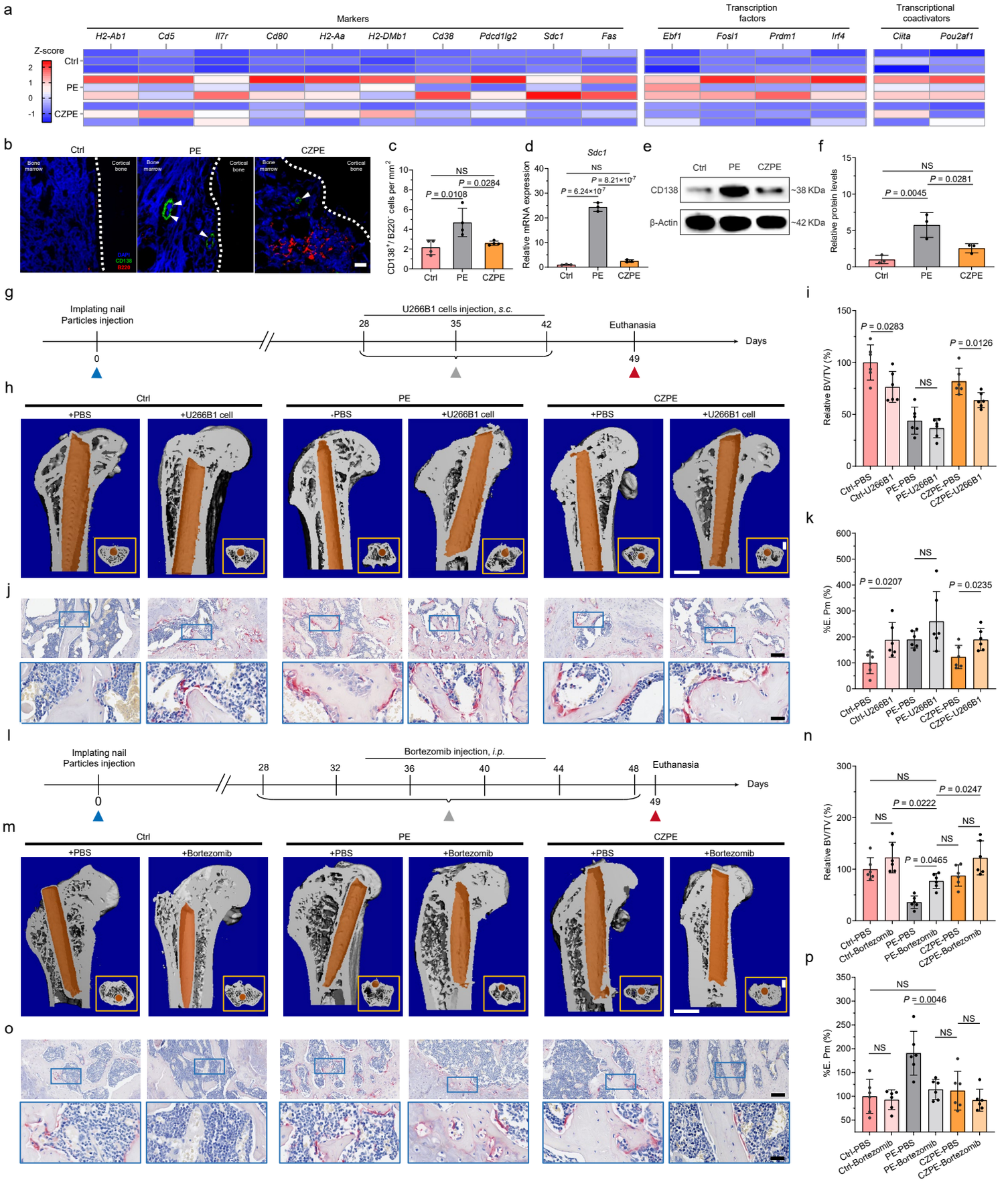
a
Markers
H2-Ab1
Cd5
Il7r
Cd80
H2-Aa
H2-DMb1
Cd38
Pdcd1lg2
Sdc1
Fas
Transcription factors
Ebf1
Fosl1
Prdm1
Irf4
Transcriptional coactivators
Ciita
Pou2af1
Z-score
Ctrl
PE
CZPE
b
Ctrl
PE
CZPE
Bone marrow
Cortical bone
DAPI
CD138
B220
c
CD138+/B220- cells per mm2
NS
P = 0.0284
P = 0.0108
d
Sdc1
Relative mRNA expression
NS
P = 8.21×10-7
P = 6.24×10-7
e
CD138
β-Actin
~38 KDa
~42 KDa
f
Relative protein levels
NS
P = 0.0281
P = 0.0045
g
Implating nail
Particles injection
U266B1 cells injection, s.c.
Euthanasia
Days
h
+PBS
+U266B1 cell
i
Relative BV/TV (%)
P = 0.0283
P = 0.0126
NS
Ctrl-PBS
Ctrl-U266B1
PE-PBS
PE-U266B1
CZPE-PBS
CZPE-U266B1
j
k
%E. Pm (%)
P = 0.0207
NS
P = 0.0235
l
Implating nail
Particles injection
Bortezomib injection, i.p.
Euthanasia
Days
m
+PBS
+Bortezomib
n
Relative BV/TV (%)
NS
P = 0.0247
P = 0.0222
P = 0.0465
Ctrl-PBS
Ctrl-Bortezomib
PE-PBS
PE-Bortezomib
CZPE-PBS
CZPE-Bortezomib
o
p
%E. Pm (%)
NS
P = 0.0046